Politecnico di Torino

Master of Science
Academic Year 2024/2025
Graduation Session November 2025

Feasibility Study of the Electron Beam Powder Bed Fusion of Molybdenum

Advisor:
Prof. Daniele Ugues

Candidate:
Altug Ancaza

Abstract

Molybdenum is a promising refractory metal for many high temperature and high stress applications due to the exceptional thermal resistance, high strength and high creep resistance. The conventional manufacturing methods for molybdenum are problematic due to the high melting point and brittle nature of the metal. Additive manufacturing is a promising technology for producing molybdenum parts since it does not require material removal, which can cause chipping for molybdenum, and additive manufacturing technologies can generate extreme heat in a very small area, which is sufficient to fuse molybdenum powders together. Powder Bed Fusion - Electron Beam (PBF-EB) method was chosen for manufacturing molybdenum parts. In this study, the main focus was on the feasibility of PBF-EB method and the effects of using the different rotation angles of the Electron Beam (EB) between the printing of each layer of the 3D parts. This study systematically investigated the feasibility of PBF-EB and the effects of different rotation angles of 67° and 90° by conducting powder analysis, top surface investigation, Archimedes density analysis, internal porosity analysis, microstructural analysis, thermomechanical analysis and the Vickers hardness test on the printed molybdenum samples and comparing the results. The results of the aforementioned analyses show that the PBF-EB technology has the potential to produce Mo parts with up to 99.37% relative density with 12.27% higher Vickers hardness with columnar grain structure. The results also show that the effects of different rotation angles between 67° and 90° rotation was minimal in many analyses. Main difference between the two rotation angles were the morphology of the top surface of the printed samples in which 90° rotation angle produced much better top surface finish while the 67° rotation angle samples had surface cavities filled with unmelted powders on the top surface.

Acknowledgements

As I finish my thesis project I would like to thank some of the people who supported me during this time period. I would like you to know that I am grateful for the support you extended to me during my studies.

Foremost, I would like to thank my thesis advisor, Prof. Daniele Ugues whose support was crucial to the success of this thesis work. His guidance throughout this research activity was one of the largest contributors to the success of this thesis activity and I am thankful for his guidance. I am also grateful for the assistance of PhD. Saadettin Cem Altiparmak and Eng. Samuele Di Sturco during my experimental activities which were essential to this thesis. Their guidance helped me through many experiments I had to perform in this thesis and I am grateful for their assistance. I also would like to thank my girlfriend, Ilke Ismailoglu who was one of my biggest supporters and motivators and allowed me to go through even the most demanding phases of this journey. To my family, I would like to thank you for your belief in me during my studies here and also for the long years of education that helped me reach this point. Finally, I would like to thank my friends for their support and their much needed cheerful distractions while I wrote my thesis.

Table of Contents

List of Tables

List of Figures

Glossary

CT

Computer Tomography

HIP

Hot Isotatic Pressing

EBM

Electron Beam Melting

AM

Additive Manufacturing

CAD

Computer-Aided Design

STL

Stereolithography

CNC

Computer Numerical Control

PBF

Powder Bed Fusion

LB

Laser Beam

EB

Electron Beam

SLS

Selective Laser Sintering

SLM

Selective Laser Melting

DMLS

Direct Metal Laser Sintering

SHS

Selective Heat Sintering

PBF-EB

Powder Bed Fusion - Electron Beam

PBF-LB

Powder Bed Fusion - Laser Beam

Mo

Molybdenum

BCC

Body-Centered Cubic

CTE

Coefficient of Thermal Expansion

TMA

Thermomechanical Analysis

AE

Area Energy

VED

Volumetric Energy Density

PSD

Particle Size Distribution

XRD

X-ray Diffraction

ONH

Oxygen/Nitrogen/Hydrogen

IGF

Inert Gas Fusion

Chapter 1

Introduction

1.1 Background of the Project

Molybdenum (Mo) is a silvery refractory metal, as it can be seen in Figure 1.1, that has exceptional mechanical and thermal properties, making Mo a promising material for many engineering applications that require materials to withstand extreme temperatures and high loads. Pure molybdenum has a crystal structure of Body-Centered Cubic (BCC) and also has defining qualities such as high melting point of 2623° C [1][2]. These unique properties of molybdenum make it a suitable material for many industries such as; alloying element in different types of iron and steel production, lighting, electrical and electronical devices, semiconductor manufacturing, nuclear, medical equipment, high temperature processing and thermal spray coatings [3][4]. The high temperature strength and thermal stability of Mo and its alloys make it a suitable material where more conventional engineering materials such as steels, nickel superalloys or titanium alloys are not able to meet the demands of the application. Despite these attributes of Mo, the inherent brittleness and the strong affinity of it to oxidation make it a challenging material for processing and shaping according to the desired applications [5].

Figure 1.1: Molybdenum Metal [6]

Molybdenum products are traditionally produced by first forming sintered ingots using powder metallurgy and sintering processes such as Hot Isotatic Pressing (HIP). These Mo ingots can be further shaped by thermomechanical methods in order to obtain rods, plates, or other desired geometries. These geometries can then be further processed by machining, fabrication and assembly into functional parts. The traditional processing methods for Mo require several steps in order to reach functional parts. Shaping of the Mo alloys is especially difficult due to tendency of Mo to chip and crack because of its high hardness. These limitations with traditional processing methods create a research interest for alternative methods for producing and shaping Mo parts. One of the emerging solutions for Mo processing is Additive Manufacturing (AM) which can significantly reduce cycle times, reduce the need for secondary operations and reduce the waste of expensive Mo material [7].

AM is defined as "a process of material joining to achieve 3D parts with desired geometries, typically layer by layer as opposed to formative manufacturing methodologies and subtractive manufacturing processes", according to ISO/ASTM 52900:2015 [8]. According to the ASTM F2792 standard, AM processes can be classified into 7 main categories according to the processes which are; binder jetting, direct energy deposition, material extrusion, material jetting, sheet lamination, vat photopolymerization and powder bed fusion [9]. These main categories are explained in Table 1.1. Powder bed fusion, which was also the main interest of this research, uses a high energy laser or Electron Beam in order to fuse the regions of the material powder layer by layer in order to obtain parts in the desired shapes.

Table 1.1: Additive Manufacturing Categories [10]

Additive Manufacturing Method	**Description**
Binder Jetting	A binding agent is deposited onto the powders inside the powder bed in liquid form. The binding agent allows selective joining of the powders to create a cross section.
Direct Energy Deposition (DED)	The printing material, for instance, a metal wire is melted by an electron or laser beam as it is deposited layer by layer to form a 3D shape.
Material Extrusion	The printing material, usually a thermoplastic filament, is forced out of a nozzle with the application of pressure in order to form layers. The material is heated in order to reduce viscosity.
Material Jetting	The entirety of the part material is jetted from a building head onto the building area in order to form layers which form the 3D shape.
Sheet Lamination	In sheet lamination thin sheets of the building material is cut, stacked on top of each other and bonded to form a 3D solid shape. Metal, polymer paper and ceramic variants exist.
Vat Photopolymerization	A vat which contains the photopolymers is subjected to radiation with the pattern of the cross section. The radiation cures the photopolymer and creates layers for the 3D shape.
Powder Bed Fusion (PBF)	The building material which is in powder form is spread layer by layer and selectively fused using a heat source in order to create layers that form the 3D shape. The heat source is usually an EB or LB.

The powder bed fusion processes mainly use either a laser or an EB for the heat source to fuse the materials. Although both of these heat sources can be used for processing Mo, the main interest of this research was using Powder Bed Fusion - Electron Beam (PBF-EB) technology to process Mo powders [11][12][13][14]. PBF-EB method involves fusing of powders due to the heat generated by the electron beam. Electron beam is generated at the cathode and passes throught a perforated anode in order to strike the powders below and generate heat. The electron beam can be manipulated using electromagnetic fields in order to move the beam on the powders according to the design parameters. The PBF-EB method involves a vacuum environment during operation since the electrons making up the beam can interact with the gas molecules inside the processing chamber and reduce the effectiveness and accuracy of the entire process. After one layer is fused using the EB, a roller mechanism spreads a new layer of powder on top of the processed powders and the fusing process continues layer by layer [15]. The PBF-EB process is a promising technology for Mo due to zero thermomechanical forces involved which can cause cracks and chipping of the Mo workpiece and the vacuum environment which eliminates the risk of oxidation of the Mo workpiece due to its high oxygen affinity. It is also possible to create complex geometries using PBF-EB which would be impossible to achieve using traditional methods such as machining due to proneness of Mo to chipping and cracking as well as general difficulty of creating complex shapes using subtractive shaping methods. A diagram of a typical PBF-EB machine can be seen in Figure 1.2.

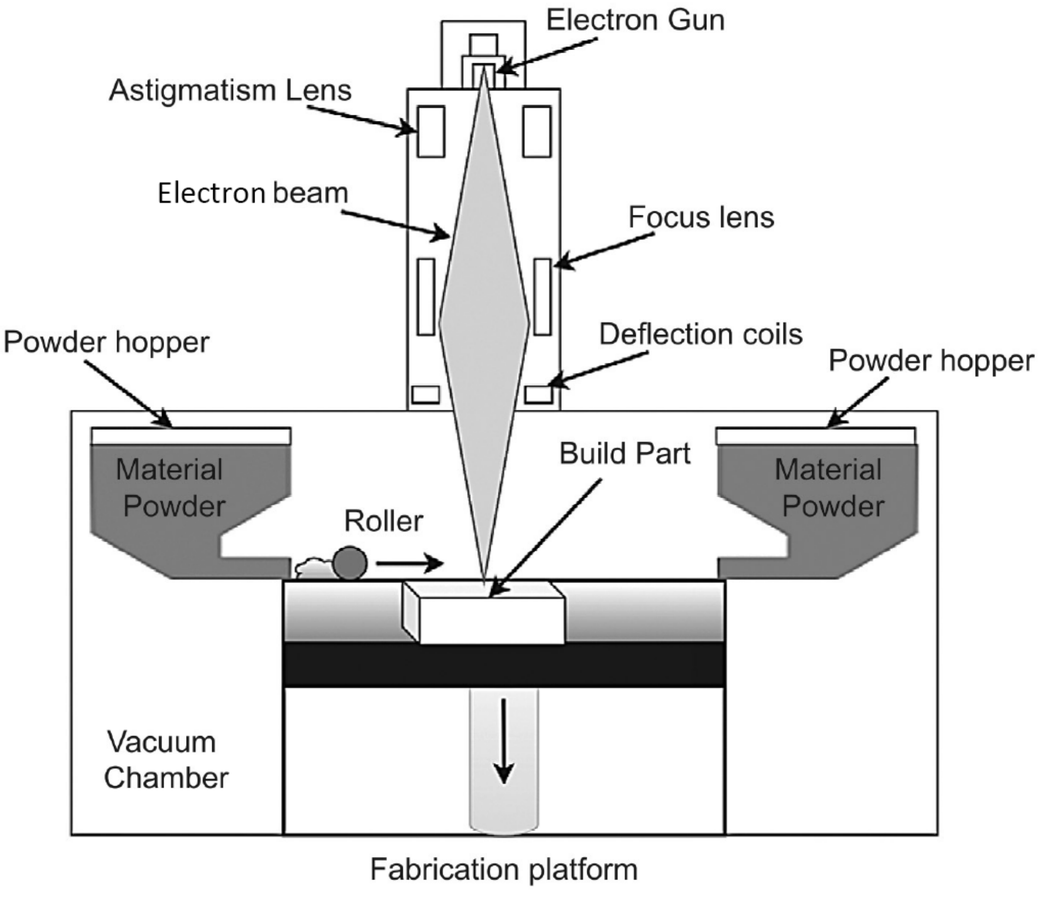

Figure 1.2: A typical PBF-EB Machine [16]

During the operation of a PBF-EB machine, it is necessary to determine a number of parameters before the building step can commence. The printing parameters of the PBF-EB machine should be selected carefully in order to achieve the best results in terms of mechanical properties, surface finish and building time. Some of the main parameters that can be selected in order to influence the results of the printing include; beam power, layer thickness, preheating temperature, line offset, beam speed and the scanning strategy of the beam. In order to achieve the best results of the printed samples, after the printing step it is crucial to optimize the mentioned parameters according to the material since each material requires different parameters for optimal results. Scanning strategy refers to how the EB will scan the unmelted powders in order to melt and fuse them. Scanning strategy is one of the most influential printing parameters and was also the main focus of this research activity. Different scanning strategies can have different outcomes in material properties including the direction of elongated grains, grain size, surface roughness, density and texture [17]. These aforementioned effects on material properties are mainly caused by the different thermal behaviors of the material due to the difference in the nature of heating and cooling effects. Different scanning strategies heat the unmelted powders in different ways which can affect the thermal behavior of the powders and the printed part during printing. It is possible to observe a difference in parameters such as, thermal gradient, direction of heat flow, cooling rate and solidification rate due to different scanning parameter usage [17] [18][19].

There are several methods in which the beam can scan the unmelted powders in the building chamber. These scanning methods can be seen in Figure 1.3. In the figure the arrows indicate the path in which the EB takes as it scans the powders inside the building chamber. The most common scanning strategies are the uni-directional (Figure 1.3a) and the bi-directional (Figure 1.3b) scanning methods in which the beam follows a long path along the length of the part, in which the only difference is the variation of the scanning vector. The island or chessboard scanning strategy (Figure 1.3c) involves dividing the building area into small squares which reduces the length of the scan vector. The varied scan strategies (Figure 1.3d and Figure 1.3e) differ from Figure 1.3a and Figure 1.3b by alternating the scanning sequences in order to change the temperature gradient. Helix scan (Figure 1.3f) which also reduces the scan vector length involves scanning the material in a way that resembles a helix. In some scanning strategies such as Figure 1.3g, Figure 1.3h and Figure 1.3j, EB changes the scanning direction between each consecutive layer. The rotation of this building direction indicated by the angle between each consecutive layer. The spot melting (Figure 1.3i) differs from other strategies since instead of scanning vectors it involves consecutively focusing the EB on a random spot on the powder surface and melting that area of the powder.

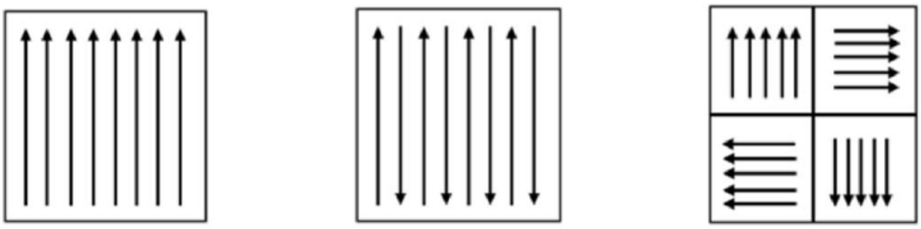

(a) uni-directional scan **(b)** bi-directional scan **(c)** island scan

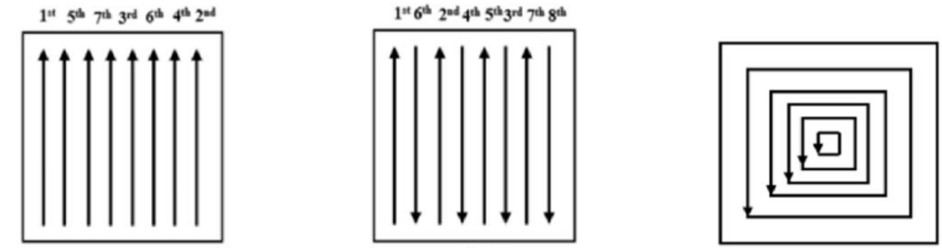

(d) uni-directional varied scan **(e)** bi-directional varied scan **(f)** helix scan

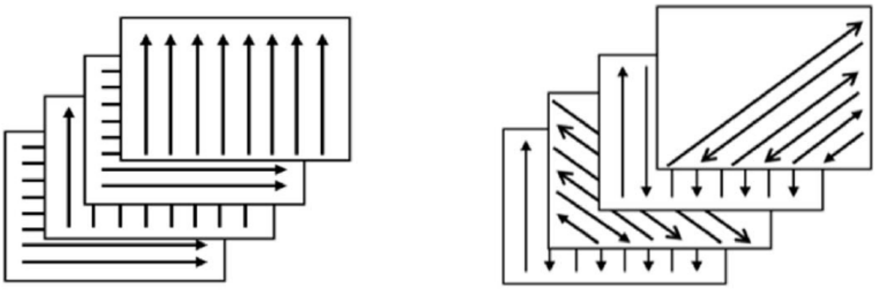

(g) 90° rotation scan **(h)** 45° rotation scan

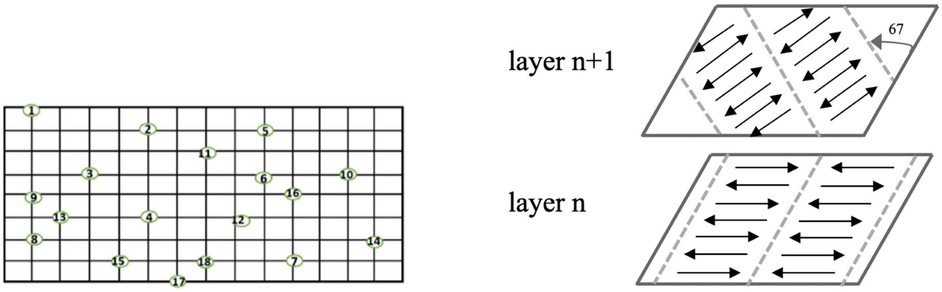

(i) spot melting **(j)** 67° rotation scan

Figure 1.3: Different Scanning Strategies for Powder Bed Fusion [17], [20]

1.2 Objectives and the Structure of the Thesis

In this research activity the main goal was to use PBF-EB method to produce high density Mo samples with comparable physical and mechanical properties to Mo parts manufactured with traditional methods. Another goal of this research was to investigate the effects of changing the rotation angle after each layer. In order to reach this goal and verify if the obtained Mo parts are comparable to Mo parts manufactured by traditional methods, the following steps and analyses were completed:

- The first step of this research activity was to characterize the Mo powders that are used to print the Mo samples in this paper. To characterize the powders, flowability tests and Hausner ratio calculations were conducted in order to better understand the flow characteristics of the Mo powders which could influence the final properties of the printed Mo parts. Next, the skeletal density analyses were conducted using a gas pycnometer in order to calculate the skeletal density of the Mo powders which could provide more information about the quality of the powders. Afterwards, the powders were investigated under the optical microscope in order to better understand the shape, morphology and any defects the powder particles may have had inside. Next, the ONH analysis was conducted in order to check the oxygen content of the starting powders which can cause gas porosities in the final Mo samples. Finally the XRD and analysis was conducted on the Mo powders in order control if the powder particles are pure and do not contain any defects that might create impurities inside the final parts.

- The Mo powders were used inside the Freemelt One PBF-EB machine in order to print the samples that were used in this research activity. A total of 4 samples were printed, in which 2 of them were printed using 90° rotation of the EB between subsequent layers and the other 2 samples were printed using 67° rotation of the EB between subsequent layers. These samples are used for investigating the effects of different rotation angles on the printed Mo samples.

- The printed Mo samples have undergone several analyses including; investigation of the top surface morphology, the Archimedes density analysis, internal porosity analysis under optical microscope, microstructural analysis with the optical microscope after etching the samples with an acidic solution, thermo-mechanical analysis in order to calculate the CTE of the Mo samples, and finally the Vickers hardness test. The aforementioned tests are conducted both with the goal of investigating the feasibility of the PBF-EB method for printing Mo samples and any differences that arise due to different rotation angles between subsequent layers.

Chapter 2

Literature Review

2.1 Additive Manufacturing

Additive Manufacturing (AM) technology, popularly called 3D printing, is defined as "a process of material joining to achieve 3D parts with desired geometries, typically layer by layer as opposed to formative manufacturing methodologies and subtractive manufacturing processes", according to ISO/ASTM 52900:2015 [8]. AM is a concept derived from Rapid Prototyping which was the initial form of AM. The rapid prototyping concept describes a fast way to create a concept or a part before actual large scale production can begin. These prototypes can form a basis for the actual product to be produced. However, the concept of rapid prototyping in its earlier definitions is not enough to describe what the recent technologies are capable of in this field. Today it is possible to directly produce many parts by using additive manufacturing machines without the need of another production method after prototyping. Another downside of the rapid prototyping concept is that it ignores the "additive" aspect of this manufacturing method [10]. As a result, the additive manufacturing concept is used in more recent standards such as ISO 52900 [8].

AM in its most simple definition works by following several steps in order to create additively produced parts. A generic AM process starts with the 3D modeling of the desired parts by using a Computer-Aided Design (CAD) software. The software enables users to describe the entire geometry of the part in the computer environment [10]. Then, the 3D model is converted into what is called a Stereolithography (STL) file format [10] [21]. Subsequently, the STL file is transferred to the AM machine which is responsible for producing the part. In the AM machine, the printing settings such as layer thickness or scanning speeds can be defined and modified. The machine starts building the desired 3D part according to the predefined design printing settings. The machine builds layers upon layers according to the layer thickness until the entire part is produced. After the building, the built part is removed from the machine and some post processing such as cleaning or removal of supporting structures may be required. After the post processing, the parts are ready to be used in aimed applications [10].

Additive Manufacturing processes all refer to production methods that fabricate parts through a layer-by-layer approach. This manufacturing approach is essentially different from more traditional manufacturing approaches that are based on material removal until the desired part is obtained [10].

There are specific merits and limitations that come with AM processes compared to more traditional 3D Computer Numerical Control (CNC) processes in which excessive amount of unwanted material is removed from the starting block. In this regard one of the main advantages of AM is to increase the production speed of the whole process by removing many of the necessary steps that would be required in the 3D CNC processes. As the design of the parts become more complex, production methods based on material removal start to require many stages to be carried out in order to obtain the desired parts. Even small design changes can lead to drastic increases in manufacturing times required in CNC processes. The speed of AM processes on the other hand are relatively insensitive to the complexity of the design as the parts are built in layers in any case [10]. The CNC processes which are based off material removal usually remove material much faster than AM processes can add material [22][23][10]. However this specific feature is only one part of the entire manufacturing step and AM processes can have less manufacturing times since all the manufacturing steps are completed in one step. Another drawback of additive manufacturing is the accuracy of the final parts. AM processes in general have much lower dimensional accuracy compared to subtractive manufacturing processes [23][22][24]. However this problem can be overcome by creating a hybrid manufacturing process which employs both AM and CNC processes. Hybrid AM processes can compensate for the drawbacks of the AM processes such as accuracy and surface finish [25][26].

Although the AM processes have the same general steps, these manufacturing processes can be classified further according to the method of creating the said layers for layered production. According to the ASTM F2792 standard AM processes can be classified into seven main categories according to process categories [9]. The first of these categories is binder jetting in which a liquid binding agent is deposited onto the substrate. Powder materials are selectively bonded together to create layers with the help of binding agents. The second AM process is a process called direct energy deposition in which thermal energy is used in order to bind materials together while they are being deposited to form layers. The thermal energy can be created by a laser, plasma arc or electron beam. Third category is the material extrusion process in which material is deposited by extruding it from the nozzle of the AM machine [27]. The fourth process is called material jetting in which droplets of the build material is jetted from the machine in order to create layers. The fifth, which is the sheet lamination process, creates layers thanks to the binding of different layers to each other. Sixth, vat photopolymerization is a process that uses a liquid photopolymer inside a vat and cures this said polymer selectively by light activated polymerization. As the last main category of AM processes, powder bed fusion works by fusing regions of powder inside a powder bed by a heat source which could be a laser, plasma arc or electron beam. The roller of the AM machine spreads layers of powder to be selectively melted in the desired regions of this powder bed, then spreads another layer of powder throughout the layer-by-layer fabrication and selectively fuses the desired regions of the powder. This powder laying and fusing process continues until the said 3D part is complete [9].

AM processes allow the production of parts that could be made from different material classes. AM was invented to be used for polymeric materials and waxes. However it is currently possible to additively manufacture various material classes such as metals, composites and ceramics. Additive manufacturing offers another unique merit in the material selection when the material hardnesses are considered. Traditional CNC processes use cutting tools in order to remove material. However hard materials such as hard metals or ceramics are really difficult to remove from the starting block. Hard and brittle materials reduce the life of the tools much faster than softer materials and materials are much more prone to chipping or cracking due to forces involved in the material removal. This makes shaping of hard and brittle materials especially difficult for CNC manufacturing. AM on the other hand does not need to remove material to shape the parts. This makes additively manufacturing hard and brittle materials by using AM methods advantageous over more traditional methods [10]. Note that Powder Bed Fusion (PBF) is the main focus of this study and will be detailed in Section 2.2.

2.2 Powder Based Additive Manufacturing

Powder based AM, also known as Powder Bed Fusion (PBF) is a manufacturing method which involves building desired parts by fusing powders layer by layer. In PBF, powders are used as feedstock [28][29]. In PBF processes the powders are fused together by heat energy by using an external heat source. The heat energy is usually imparted by a Laser Beam (LB) or an Electron Beam (EB) [28][29]. Both processes work similarly spreading the material powder layer by layer and selectively melting powders with the energy provided by the EB or LB. The main difference between the two processes is that EB requires a vacuum atmosphere and the powders are preheated using the EB [30]. Monochromatic and coherent light beam supplied by the laser can be used to heat up multiple material types such as metals and polymers [28][31]. Electron beams on the other hand generate a spot size far smaller than a typical laser and can be focused and rapidly steered by electromagnetic lenses. The rapid steering of the beam allows precise control of position and melt pool size [32].

Main PBF processes can be classified into five categories which are Selective Laser Sintering (SLS), Selective Laser Melting (SLM), Direct Metal Laser Sintering (DMLS), Selective Heat Sintering (SHS) and Electron Beam Melting (EBM). SLS involves spreading of the powders using a roller mechanism. A powder delivery piston moves up in order to create a steady supply of powders for spreading. Each instance of a piston movement is followed by the roller spreading the powders. After the powders are spread, the laser can selectively scan and sinter the powders based on the CAD data, forming a sintered layer. After the sintering of the first layer the part building bed moves down to enable spreading of a new powder layer on top of sintered parts using the roller and powder delivery piston. The sintering process continues following this sequence until the part is finished [33][34][35]. The SLS process is typically used for polymer powders, for metal powders a low melting point metal is used to melt and bond with higher melting point powders [33]. SLM process is similar to SLS, however in SLM the powder particles are completely melted rather than sintered. The melting process reduces manufacturing cycle times and can form finer microstructure due to more rapid cooling [33]. Parts produced by SLM process also have better mechanical properties compared to parts produced by SLS method [17][36]. The DMLS is similar to SLS and Selective Laser Melting (SLM) methods in which metal alloy powders are heated up just enough to sinter together in order to form the desired shape [37]. In SHS process the plastic powder particles are spread and selectively melted following the spreading of the plastic powders by using a heated head by touching the powders [38].

The last method for PBF processes is the Powder Bed Fusion - Electron Beam (PBF-EB) process which will be discussed more in detail in Section 2.3. The PBF-EB has a similar setup to the SLM process with the EB selectively melting the powders in order to create layers which continuous creation of new layers ultimately leading to the finished parts [39]. There are several distinctions of PBF-EB processes to the PBF-LB processes which include difference in (i) powders used, (ii) energy efficiency of the beam, (iii) powder-beam interactions, (iv) movement of the beam and (v) the vacuum environment. In PBF-EB, the mechanism of the process requires powders to be electrically conductive in order to disperse the charge created by the electron beam on the powders whereas in SLS there is no requirement for powders to be conductive in PBF-LB processes. Due to this conductivity requirement of the powder PBF-EB process mainly uses metal and metal alloy powders. Another distinction between PBF-EB and PBF-LB is that electron beam is much more energy efficient in terms of electrical energy consumption per gram of material. The electron beam can build almost 3 times as much material for the same amount of energy consumed [40]. This is due to high energy conversion energy of the electron beams compared to lasers. There is also a distinction between the way EB and LB interact with the powders as previously discussed. EB consist of electrons which get deflected by the free electrons that surround the powder atoms. When the beam is sufficiently powerful these electrons will penetrate deeper inside until these atoms are decelerated by the lattice atoms. This deceleration creates an energy transfer in which kinetic energy of the electron is transferred to the lattice atom which causes lattice atom to vibrate and generate heat which causes the melting [10][15]. Lasers on the other hand consist of focused photons which interact with the surrounding free electrons of powder atoms. If there is a high number of free electrons the chance of photon to be reflected increases. In the case of laser beam with sufficient intensity, if radiated to the powders, there is a higher chance that the photons will interact with the bound electrons which can re-radiate or interact with the lattice atoms to create vibration [10][15]. Another aspect of the EB is that it can provide scan speeds several times higher than LB machines [41]. Finally the PBF-EB machines work in vacuum conditions compared to LB machines which generally do not utilize vacuum environment. The vacuum environment is essential to the PBF-EB machines [15][10].

2.3 Powder Based Additive Manufacturing Using Electron Beam Melting

PBF-EB involves fusing of powders using an electron beam. The electron beam is generated by heating an electrode made from high melting point elements with low work function named the cathode. High melting point ensures that the cathode neither melts or degrades during electron generation while low work function makes it easier for electrons to detach from the cathode at lower voltages [15]. Work function is a term that states how much potential difference needed in order to detach electrons from a material [42]. The cathode material typically made out of tungsten (W) or lanthanum hexaboride (LaB_6) [43][15]. LaB_6 is typically used due to its low work function while W is preferred mainly for its high melting point [44]. The generated electrons move towards a positively charged anode and these electrons constitute the electron beam. The electron beam generated at the cathode passes through a perforated anode and strikes the powders below the anode and cathode in order to generate heat. The beam size is generally in the order of millimeters. Due to the charged nature of the generated electrons, the EB can be manipulated by using electromagnetic fields and the EB can be moved. How far and how fast the EB moves is directly correlated to the magnitude of the magnetic field. The focusing of the EB can also be achieved by the magnetic field. EB systems operate in vacuum environment which is essential to the functioning of the system. For instance, in Freemelt systems the vacuum environment of 10^{-5} mbar is maintained [45]. Without the vacuum environment the interaction of electrons with air molecules results in the ionization of the molecules, thus losing speed, direction and energy. Another advantage of the vacuum environment is that it makes processing of reactive elements easier than air atmosphere systems since the reactive elements cannot react with the gasses in the air [15]. The majority of the kinetic energy of the electrons are converted into heat which is the main heat source for sintering and melting [46]. Spreading of the powders layer by layer can be achieved using a metallic blade, a roller or a rake in order to create even and precise layers [47]. A schematic of a typical Powder Bed Fusion - Electron Beam machine can be seen in Figure 2.1. The size of the building area of the typical PBF-EB is usually in the order of few hundred millimeters in diameter and a few hundred millimeters in height for manufacturers such as Arcam and Freemelt [45][48]. The beam power of these machines are adjustable according to the needs of the project and the machines can supply up to 3-6 kWs of energy for the electron beams [45][48].

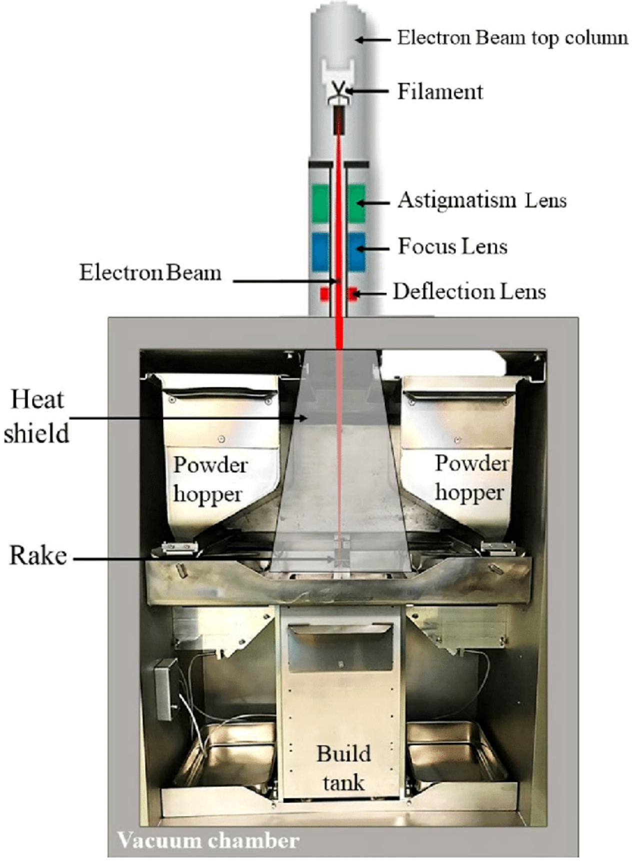

Figure 2.1: Typical PBF-EB Machine [49]

The powders are preheated by scanning the powders with the EB or external heaters which creates limited sintering and necking between the powders [30][15]. For instance, for processing copper, a preheating temperature of 400° C is used [50]. Preheating of the powders prevents the so-called smoke effect which mainly occurs due to loosely packed particles becoming negatively charged and repulsing each other. In the case of repulsion forces being stronger than the weight of the powders, an explosion like event of powders can occur and the whole process chamber can be contaminated with the powders [51][52]. The role of the neck is mainly to act as a conduit for charge transfer rather than being an actual fixture to hold the powders together. Formation of the neck helps with the dissipation of the charges to the ground. In order to achieve further powder stability, large diameter powders are used due to their high inertia which reduces the chance of repulsion during charging [53]. In PBF-EB machines, usually after the preheating is achieved inside the PBF-EB machine, layer by layer production of the desired part can be completed by selectively melting the powders using the EB. During the melting process peak temperatures up to 3000 K can be reached due to high energy intensity and superior absorption of the EB processes [54].

In PBF-EB machines, the powders used typically contains spherical particles. Spherical particles are preferred due to their superior flowability and packing density. Spherical powders can easily roll over each other, reducing friction, during spreading process due to their shape when compared to irregular particles. Additionally, the spherical particles exhibit much higher packing densities when compared to irregular shaped particles. High packing density affects the density of the finished product as well as mechanical properties of it [55][56]. The sizes of the powders range between a couple of μm up to a few hundred of μm [55][57]. For instance, Molybdenum (Mo) powders that are used for additive manufacturing that are produced by Stanford Advanced Materials are spherical and have particle sizes between 1 μm and 45 μm [58].

2.4 Powder Based Additive Manufacturing Using Electron Beam Melting Of Different Metals

The PBF-EB process is mainly applied to pure metals and metallic alloys. Since pure metals are rarely applied in the industry, the majority of applications are limited to metallic alloys. However, applications of pure metals exist as well, such as; pure titanium for medical applications, pure copper for its electrical properties, and pure niobium for its superconductive properties. When using the powders of the aforementioned materials it is possible to reach 100% density with the correct processing parameters for the PBF-EB machine. It has been shown that parts produced with the PBF-EB machine can achieve mechanical properties similar to to or even superior to materials produced by forging [59]. The reason is that the PBF-EB process involves extremely fast cooling rates compared to wrought alloys, resulting in finer microstructures, improving mechanical properties [60].

Some of the initial materials used for the PBF-EB process are pure iron and steel. Murr et al. used PBF-EB process for producing pure iron parts and they were able to obtain parts with 96% density with ultimate tensile strength of 170 MPa [61]. Botero et al. investigated the properties functionally graded material which combined stainless steel and tool steel powders in PBF-EB process. They were able to obtain metal parts that included no cracks or significant porosity with a continuous transition between stainless steel and tool steel regions [62]. Segura et al. investigated the production of 316L stainless steel alloy with PBF-EB. The team reported a 76% increase in yield strength and a 29% increase in ultimate tensile strength when compared to wrought alloys [63].

The majority of PBF-EB research is being conducted on titanium and titanium alloys especially the Ti-6Al-4V alloy. The processing of titanium with traditional methods are often difficult due to high reactivity of titanium with oxygen. The vacuum conditions of the PBF-EB makes this processing method a major research interest for developing production methods for titanium and its alloys. Davids et al. produced Ti-6Al-4V alloy samples in the form of 15×15×25 mm prisms by using spherical powders with the size distribution ranging from 45 μm to 105 μm. The Ti-6Al-4V samples produced with PBF-EB method were able to reach slightly higher hardness levels compared to traditional methods [64]. Shao et al. compared the effects of beam scan strategies on Ti-6Al-4V samples. The team used a standard build setting which include 60 kV accelerating voltage, 4.5×10^{-2} mBar vacuum, 1200 W beam power, 743 K preheating and 50 μm layer thickness. The scan strategies which were investigated include linear raster scan, ordered spot scan and random spot scan. The team reported significant variations in micro-structural features when using different scan strategies but did not investigate mechanical properties [65]. Pan et al. investigated the effects on manufacturing methods on Ti64–TiBw composites. The composites were prepared with 5.1 vol% TiBw and the rest is Ti-6Al-4V. The composites produced with PBF-EB showed 28% higher tensile strength when compared to composites produced by forging. The PBF-EB samples also showed superior elongation at break values with almost 81% increase in elongation [66]. Murr et al. also reported an 23% to 92% increase in elongation levels [67].

Another major interest for PBF-EB research is the nickel alloys. Nickel alloys show excellent mechanical properties with high creep and oxidation resistance. In nickel based alloys PBF-EB offers a distinct advantage against SLM by being more suitable to producing non weldable nickel alloys due to the fact that it is possible to preheat the powders up to 1100 °C [59]. Luo et al. investigated the production of Inconel 738 nickel super alloy with PBF-EB technology. The team used two different scanning methods which are linear and random scan methods. The build parameters used were; 50 μm layer thickness, 60 kV accelerating voltage, 1000 °C preheating, 75 μm hatch spacing for linear scan and 960 W beam power. The team reported that scan strategy greatly alters microstructure and observed that the random scan technology showed finer grains and better mechanical properties [68]. Knapp et al. investigated the solidification structure of Inconel 718 alloy in their research. For the production of the samples with PBF-EB they used following process parameters; 60 kV beam voltage, 400 μm beam radius, 50 μm layer thickness, 1200 W beam power and 0.25 ms time beam-on. The team used a pulsed beam scanning strategy for producing the alloys [69]. Yao et al. investigated the properties of Ni_3Al alloy at room temperature and elevated temperatures. The team was able to produce Ni_3Al alloy using PBF-EB which had around 560 MPa ultimate tensile strength at 1000 °C [70]. Hinojos et al. investigated joining Inconel 718 and 316L stainless steel. The build parameters they used for Inconel were; beam speed of 918 mm/s, 12 mA beam current, 22mA beam focus, and fabrication temperature of 920 °C [71].

2.5 Molybdenum

Molybdenum is a naturally occurring element found in the crust of the Earth. It is classified as a transitional metal or transitional element with an atomic number of 42 [72][73]. This metal can also be classified as a refractory metal due to its high melting temperature. 5th and 6th groups in the periodic table are where the refractory metals are found in. Refractory metals excel with their high resistance to temperature and high melting point in which their melting point can reach up to 2000 °C [2]. Molybdenum can be described as a silver colored metal. It has the 6th highest melting point out of any element in the periodic table with a melting point of 2623 °C [1][72].

Because of its properties, molybdenum is employed by many different industries. Molybdenum is mainly used as an alloying element in different types of iron and steel production and as well as chemicals industry. Steel and chemical industries make up about 84% of the molybdenum usage [74]. Other usage areas of molybdenum include lighting, electrical and electronical devices, semiconductor manufacturing, nuclear, medical equipment, high temperature processing and thermal spray coatings [3][4][75].

In the lighting industry, the molybdenum is mainly used as support wire and glass feed-throughs in halogen lamps for its high temperature resistance and ability to withstand thermal stresses. In electrical and electronical devices, molybdenum can be seen in electron vacuum tubes as filament support and grids for its high temperature strength and stability. Semiconductor industry also employs molybdenum as a component in ion sources for its resistance against high temperatures during doping processes. In medical industry, molybdenum is used in X-ray tubes that can be commonly found in Computer Tomography (CT) machines. In metal processing at high temperatures, molybdenum is also employed due to its high temperature strength such as hot work tools used in steel production. Another example is the usage of molybdenum as construction material in vacuum furnaces and in Hot Isotatic Pressing (HIP) machines. Thermal spray coatings using Molybdenum as spray material can also be found for using this metal to create new surfaces on different materials [3]. Another possible use for molybdenum is the nuclear energy sector. Molybdenum or molybdenum based Titanium-Zirconium-Molybdenum (TZM) alloys are used in the nuclear sector as; early potential fuel pin cladding material, turbine components, fuel refinement systems and power converter systems. Molybdenum and other refractory materials are also planned to be used as containment systems for future fusion reactor projects [76].

Table 2.1: World Mine Production and Reserves of Mo Metal per Country [77]

	Mine production (metric tons)		Reserves
Country	2023	2024	(1,000 metric tons)
United States	34,000	33,000	3,500
Armenia	7,600	8,000	150
Australia	660	1,000	1,600
Canada	1,150	1,200	640
Chile	440,000	380,000	190,000
China	96,100	96,000	5,400
Iran	2,500	3,000	43
Kazakhstan	3,730	3,900	7
Korea, North	300	700	NA
Korea, Republic of	339	300	18
Mexico	17,600	17,000	130
Mongolia	3,160	1,700	30
Peru	33,500	41,000	1,900
Russia	1,700	1,700	1,100
World total (rounded)	248,000	260,000	15,000

Molybdenum occurs in the Earth's crust as metal sulphides and extracted as such. World's total mine production of Molybdenum in 2024 was 260.000 tons with the main producers being China, Peru, Chile and The United States. A detailed breakdown of Mo production and Mo reserves can be seen in Table 2.1. Identified resources of Molybdenum are around 20 million tons dispersed around the world

[77]. Molybdenum metal production is mainly done by powder metallurgy with powder metallurgy having 95% of the production share. The rest is produced by more recent technologies such as vacuum arc melting and Electron Beam Melting (EBM) [78].

2.6 Powder Based Additive Manufacturing Using Electron Beam Melting of Molybdenum and Molybdenum Alloys

The production of Mo parts through the use of PBF-EB technology is of recent research interest. As discussed in Section 2.5, molybdenum has a wide range of uses in several industries such as electronics, nuclear energy, and coatings. Although research regarding the production of Mo parts with PBF-EB is limited due to the recency of this field, there are several research projects done investigating the viability of PBF-EB for Mo production. These research projects focus on several aspects of the PBF-EB production of Mo such as the optimal process parameters, density of the produced parts, mechanical properties of the produced parts and the microstructure of the Mo samples.

Di Sturco et al. investigated the processability, mechanical properties, and final microstructure of the Mo parts produced by PBF-EB. The team used a Freemelt ONE PBF-EB machine to produce the Mo parts for the investigation. The process parameters used is as follows; accelerating voltage of 60 kV, vacuum level of 10^{-5} mbar to 10^{-6} mbar without a process gas, layer thickness of 0.07 mm, beam power of 1080 W, 1175 °C preheating temperature, 400-700 mm/s beam speed, 10-12 mm line offset between each scan and a scanning strategy which involves 90° rotation of the beam between each consecutive layer. The resulting Mo samples had high density levels reaching to 99.85% relative density. Mechanical property tests were also conducted on the Mo samples, with results that were compatible or with those of the traditionally produced Mo samples. Microstructure of the samples included a strong <001> texture with columnar grains along with <110> texture perpendicular to the direction in which samples are produced [12].

Zelaia et al. used an Arcam Q10+ EBM Machine in order to fabricate pure Mo parts. For this investigation the researchers used 1300 °C preheating temperature and a relatively tight line ofset of 86.755 μm. The beam power was alternated between 540 W and 720 W for different trials. End results were promising with relative densities reaching up to 99.9% compared to pure molybdenum. For majority of the parts the microstructure texture had a <001> texture with some samples also having <111> texture. The team did not conduct any mechanical property investigations on the samples produced with PBF-EB method [14].

Chapter 3

Methodology

In this chapter, the devices and methods used in order to obtain the results of this research were discussed. This section chronologically explains the steps from powder characterization to the analytical analyses performed on the printed Mo samples. The details include the type of devices used, the parameters used during the operation of the said devices, software used in order to analyze the samples and the analytical calculations employed during the research.

During this research a total of 4 Mo samples were printed using pure Mo powders that were supplied from Metalpine [79]. The Freemelt One PBF-EB machine is used for creating the four Mo samples that were used in analyses [45]. Two of the samples were printed using 90° rotation of the EB between subsequent layers and the other two samples were printed using 67° rotation of the EB between subsequent layers. The 90° rotation samples were named 90-001 and 90-002 and the 67° rotation samples were named 67-001 and 67-002. The samples with the same rotation angle were all printed using the same parameters during the same printing cycle.

3.1 Powder Characterization

3.1.1 Flowability Test

For the PBF-EB technology, the quality and the properties of the powders are crucial. One of the main properties that define the printing powders is the flow rate of the said powders. The determination of the flow rate of the metal powders were achieved by the Hall and Carney flow rate tests [80][81]. Carney and Hall flow rate tests are performed similarly, in which a weighed mass of powders is placed inside a test cup and, the time it takes for powders to flow through an orifice underneath the test cup is recorded. The difference between the two flow rate tests is defined by the diameter of the orifice underneath the test cup. The Carney test has a larger orifice and the test is only used if the powders cannot flow through unaided in the Hall test. During this study, in order to determine the flow rate, Hall test was used initially. However, the Mo powders were unable to flow through the Hall flow rate setup. The Carney setup was used in order to determine the flow rate of the samples. The setup which is visible in Figure 3.1 consists of a stand and a funnel which has an orifice underneath with the diameter of 5.08 ± 0.13 mm. 50 grams of Molybdenum powders were weighed and placed inside the Carney flow rate setup. The orifice underneath was then opened while recording the time it took for all of the powders to flow through the test setup. A total of five measurements were taken with the same setup in order to calculate the mean of the flow rate setup. The flow rate was then reported.

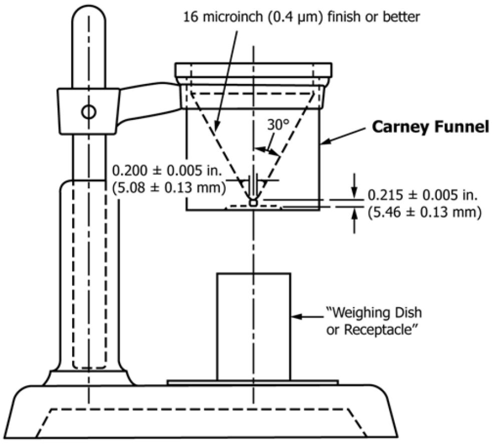

Figure 3.1: Carney Flow Rate Test Setup [80]

3.1.2 Hausner Ratio Calculation

Another property that characterizes the powders that are used in printing operations is the Hausner ratio of the powders. Hausner ratio is a measure of interparticle cohesive forces and the flowability of the powders. The Hausner ratio is calculated by dividing the apparent volume of the powder particles to their tap volume. The ratio is then compared to a reference table, that can be seen in Table 3.1, in order to determine the flow characteristics of the powders [82]. The apparent volume is obtained by measuring the volume the powders occupy in their unpacked and loose state. The tap volume, on the other hand, is obtained by measuring the volume the powders are occupying in their packed or dense state. In this research activity, in order to calculate the Hausner ratio, a graduated cylinder was filled with 50 grams of Mo powder and the volume was recorded by using the grades on the cylinder. The cylinder was then subjected to vibrations by a vibrating plate for 10 seconds and the tap volume after the vibration was recorded. The tap and apparent volumes were measured for a total of three times for the Hausner ratio calculation.

Table 3.1: Hausner Ratio Reference Table [82]

Flow Character	**Hausner Ratio**
Excellent	1.00–1.11
Good	1.12–1.18
Fair	1.19–1.25
Passable	1.26–1.34
Poor	1.35–1.45
Very poor	1.46–1.59
Very, very poor	>1.60

3.1.3 Skeletal Density Analysis

In order to accurately measure the density of the powder particles that were used for the printing, the skeletal density analysis was conducted. The skeletal density is defined as the weight of the powder divided by its skeletal volume. The skeletal volume is the volume of the solid particles and the internal porosities but it does not include the volume of the interparticle voids or the volume of the open pores of the sample. The skeletal volume is much more accurate for the powder particles when compared to bulk or tap volume measurements since these values cannot eliminate the volume of the interparticle voids and the open pores. In order to measure the skeletal volume of the powder particles, a gas pycnometer was used which is able to calculate the skeletal volume by using the Boyle Law [83]. The mechanism in which the gas pycnometer works involves sealing a powder sample with known mass inside a chamber and introducing an inert gas such as helium to the environment at a predetermined pressure. Due to the small size of the helium atoms these atoms can easily penetrate in between the powder particles and the open pores. The helium gas is then subsequently vacuumed out to another chamber with a known volume and the resulting pressure is measured by the pycnometer. By analyzing the pressure change, it is possible to calculate the volume of the open voids inside the powder sample through Boyle Law. In this research activity, Ultrapyc 5000 gas pycnometer which is visible in Figure 3.2 was used in order to determine the skeletal density. A total of 35.7099 grams of Mo powder was weighed which roughly occupies 2/3 of the volume of the pycnometer cell and was placed inside the pycnometer chamber which was 20 °C inside. The target pressure for the Helium gas was then set to 0.69 bars and the flow mode was selected as fine powder. The pycnometer was used for a total of fifteen density measurements for the mean and standard deviation calculations.

Figure 3.2: Ultrapyc 5000 Gas Pycnometer [84]

3.1.4 Powder Particle Characterization

Next step for the powder characterization is investigate the shape, morphology and the particle size distribution of the powder particles. The shape and the morphology of the powder particles were investigated by using the Leica DMI 5000 M optical microscope which is explained more in detail in subsection 3.3.6. In order to prepare the powder particles for investigation and imaging under the microscope, the powder particles need to be mounted inside a polymeric resin which allows handling of the powder during imaging and polishing. For the mounting of the powder particles, the Remet IPA 30 hot mounting machine was used which will be further explained in subsection 3.3.4. After mounting the powder particles with the resin, the particles need to be polished for investigation. They are polished using the Presi Mecatech 234 polishing machine in which further information can be reached in subsection 3.3.5. The powder particles were polished using 1200, 2000 and 4000 grit polishing papers and finally the 0.25 μm silica suspension. The powder particles were then imaged under the optical microscope at 200× for determination of the morphology and the shape of the Mo powder particles. The particle size distribution of the powder particles is another analysis that was conducted. The Particle Size Distribution (PSD) of the powder particles was analyzed by a Mastersizer 3000 Laser Diffraction Particle Size Analyzer which is visible in Figure 3.3 [85]. The powder flow through an internal chamber inside the particle size analyzer and their sizes are calculated by the diffraction angle of a laser beam that hits the powder as they flow through the chamber. The instrument provides the PSD curve and the relative D_{10}, D_{50} and D_{90} values. These values indicate the diameter below which a certain percentage of the powder particles fall in. During this study 50 mm^3 of Mo powder was used for determining the PSD of the powder.

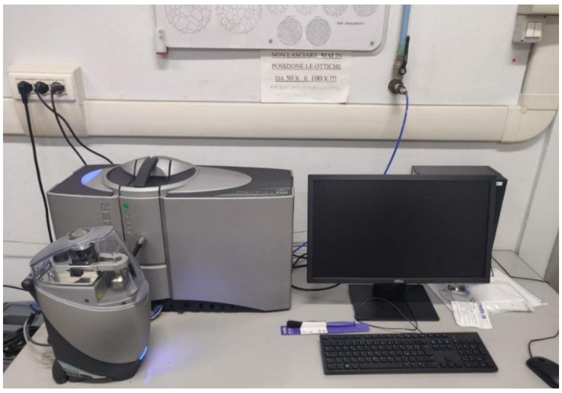

Figure 3.3: Mastersizer 3000 Laser Diffraction Particle Size Analyzer

3.1.5 Composition Analysis for Powder Particles

Next analysis that was conducted in order to characterize the powder particles is the X-ray Diffraction (XRD) analysis which allows the identification of the composition of the Mo powders. XRD is a non destructive technique particularly used for identifying the crystalline phases that make up the powder particles. The XRD machine fires a monochromatic X-rays to the sample inside the chamber of the machine and these X-rays are then diffracted by every atomic plane that makes up the material. These diffracted X-rays can constructively interfere with each other following the Bragg's Law (Equation 3.1) and reinforce each other which makes signals strong enough to be detected. Even though every atomic plane diffracts the X-rays and produce secondary waves, only the waves that originate from specific θ angles can reinforce each other to produce a peak point in the return signal. These signals are constructed as a graph that shows the specific peaks in the return signal and which θ angle these peaks originate from. These peaks are a fingerprint for every material and unique in nature. This allows the identification of the materials by comparing the specific peaks that are obtained by the XRD analysis to an existing database. In this research activity, a small batch of powder samples were analyzed by Empyrean, Serie III, Malvern Panalytical XRD machine which is visible in Figure 3.4 [86]. The return signal that was obtained by the XRD machine was then compared to the material database for identifying if the powder batch that was used for printing the Mo samples was indeed pure Mo or if there were any impurities present. The presence of impurities can create internal defects inside the printed samples and it is crucial to know the composition of the powder before proceeding with the printing.

$$2d\sin\theta = n\lambda \tag{3.1}$$

Table 3.2: Parameters of Eq. 3.1

Symbol	Description
d	distance between atomic planes
θ	incident angle
n	order of reflection
λ	wavelength of the X-rays

Figure 3.4: Empyrean, Serie III, Malvern Panalytical XRD Machine [86]

3.1.6 Powder Oxidation

Another crucial aspect of the initial Mo powder is its oxygen content. The oxygen content of the virgin powders can be determined by Oxygen/Nitrogen/Hydrogen (ONH) analyses. ONH analysis is an elemental analysis method which is useful for determining the exact concentrations of Oxygen, Nitrogen and Hydrogen content of the inorganic samples. The oxygen content of the Mo powder is especially important since any trapped gas content can lead to the formation of spherical gas porosities in bulk samples. The trapped gasses can expand during the PBF-EB process and leave behind spherically shaped voids inside the bulk samples. The analysis was conducted through the inert gas fusion method in which a weighed sample is melted inside a graphite crucible and the released gasses are detected by a detector. During this research activity, in order to determine the oxygen content of the initial Mo powder, Leco ONH 836 analyzer was used which can be seen in Figure 3.5 [87].

Figure 3.5: Leco ONH 836 Analyzer[87]

3.2 Freemelt ONE PBF-EB Machine

Freemelt ONE is a type of PBF-EB machine tailored for research and development. The machine uses a high energy EB in order to create the heat required to fuse the powders inside the building chamber of the machine. It offers an open source software which allows researchers to change the building parameters as desired. The Electron Beam (EB) source inside the Freemelt One is a diode type source along with a laser heated cathode. This source can offer a beam power between 0-6 kW with a beam acceleration voltage of 60 kV. The building chamber is in the shape of a cylinder with a diameter of 100 mm and a height of 100 mm. The building chamber is a vacuum environment as the electron beams require a vacuum atmosphere in order to not be affected by air particles in the building chamber. The base pressure inside the building chamber is 10^{-6} mbar. An image of the Freemelt One machine can be seen in Figure 3.6.

Figure 3.6: Freemelt ONE PBF-EB Machine [45]

During this research activity both the 90° and 67° rotation angle samples were printed with the same process parameters with only difference between them being the rotation angle of the EB. The process parameters which were used for all four samples can be seen in Table 3.3. The Table 3.3 also reports the Area Energy (AE) and Volumetric Energy Density (VED) values for the given process parameters. VED and AE parameters are calculated by the Equations 3.2 and 3.3. Parameters and the descriptions of the Equations 3.2 and 3.3 can be seen in Table 3.4.

Table 3.3: Processing Parameters for the PBF-EB machine

Beam Power (W)	Beam speed (mm/s)	Line offset (mm)	Layer thickness (mm)	AE (J/mm^2)	VED (J/mm^3)
1080	400	0.12	0.07	22.50	321

Symbol	Description
v	Scan Speed (mm/s)
h	Line Offset (mm)
t	Layer Thickness (mm)

Table 3.4: Parameters of Eqs. 3.2 & 3.3

$$\mathrm{VED} = \frac{P}{v \cdot h \cdot t} \tag{3.2}$$

$$\mathrm{AE} = \frac{P}{v \cdot h} \tag{3.3}$$

3.3 Printed Sample Preparation and Analysis

3.3.1 Stereo Microscope

After the printing of the samples was completed with the Freemelt One machine, the samples were examined using a stereo microscope. Stereo microscope is a useful tool for studying the surface characteristics of the printed samples. It is possible to observe the surface finish, surface porosity, unmelted powders and possible cracks. Stereo microscopes are easy to use since it is possible to use them without the need of mounting and finishing the samples. The stereo microscope used in this study is a Leica EZ4 W model stereo microscope [88]. EZ4 W microscope offers magnification levels ranging between 8-35× magnification. The microscope was used the take images at different magnification levels of the surface finish and unmelted powders during this study. An image of the Leica EZ4 W stereo microscope can be seen in Figure 3.7.

Figure 3.7: Leica EZ4 W Stereo Microscope [88]

3.3.2 Cutting Machine

After the stereo microscope imaging of the surface of the printed Mo samples, a more in depth analysis can take place. In order to evaluate the entirety of the Mo samples, investigation of the cross section of the samples is crucial. In order to access the cross section of the Mo samples, the samples need to be cut in half by using a cutting machine. During this study, a Mecatome T210 cutting machine is used in order to cut the samples in half. An image of the Mecatome T210 cutting machine can be seen in Figure 3.8.

Figure 3.8: Mecatome T210 Cutting machine [89]

Due to the high hardness of the Mo metal, a disk-shaped diamond-coated blade was used during the cutting action. The samples were mounted inside the chamber of the cutting machine along the building direction. This direction was chosen in order to investigate the any changes that might occur between the printing of consecutive layers. During the cutting action, a blade rotary speed of 3200 rpm was used. The feed rate was kept relatively low at 0.02 mm/s due to instabilities that occurred at higher cutting speeds. An image of the mounted sample and the cutting blade can be seen in Figure 3.9

Figure 3.9: Cutting blade and the Mo sample

3.3.3 Archimedes Density Analysis

Archimedes density analysis was conducted on one of the halves obtained after the cutting for each sample. Archimedes density analysis aims to measure the density of an irregular sample in which the volume of the sample cannot be calculated through theoretical means. The volume of the object is instead derived from the volume of water it displaces when it is submerged in water. The samples were weighed in dry and submerged conditions using a precision scale and a setup specifically created for Archimedes density analysis. After noting the measured weights, it is possible to calculate the volume of each sample. Volume of the sample can be calculated by considering the density of the water, 1 g/cm^3 and the weight of each sample in submerged condition. The volume of the sample can be calculated by simply subtracting the submerged weight from the dry weight. Following the density calculation for each sample, the relative density can be calculated by comparing it with the density of pure Mo, which is 10.223 g/cm^3 [90]. The formula used for density calculation can be seen in Equation 3.4. The experimental setup used during the Archimedes density analysis can be seen in Figure 3.10.

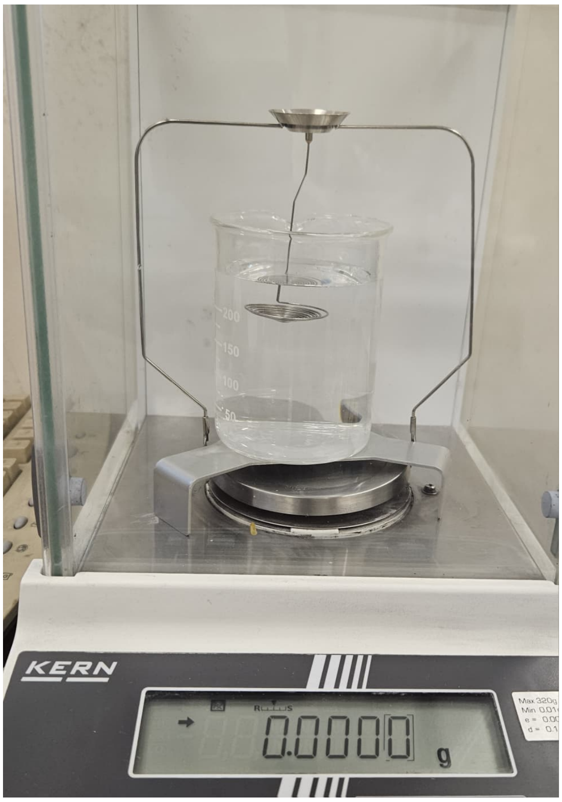

Figure 3.10: Archimedes Density Analysis Setup

$$\rho_{\text{obj}} = \frac{W_{\text{dry}}}{W_{\text{dry}} - W_{\text{submerged}}} \cdot \rho_{\text{fluid}} \tag{3.4}$$

Table 3.5: Parameters of Eq. 3.4

Symbol	**Description**
ρ_{obj}	Density of the object
W_{dry}	Weight of the object in air (dry weight)
$W_{\text{submerged}}$	Apparent weight of the object when submerged
ρ_{fluid}	Density of the fluid

3.3.4 Hot Mounting Machine

One of the most crucial steps in order to observe the cross section of the cut Mo samples is the mounting of the samples using a hot mounting machine. The hot mounting machine allows an equal polishing of the samples on subsequent steps and also allows easy handling of the samples during optical microscope imaging. The optical microscope imaging is extremely difficult without mounted samples. During the mounting of the cut Mo samples, Remet IPA 30 hot mounting machine was used which is visible in Figure 3.11. The machine has a heating chamber with a diameter of 30 mm in which the mounting operation takes place. The cut Mo samples were placed at the bottom of the heating chamber, which is a platform that can be lowered by the controls on the hot mounting machine. After the Mo samples were placed and the platform was lowered, the chamber was filled with enough thermoplastic polymer granules to cover the samples completely, giving enough leverage to grip the samples. After placing the sample and the polymer inside the heating chamber, the machine performed a thermal cycle in which it heated up to 160 °C and cooled down to room temperature for solidification. The entire thermal cycle took around 20 minutes. During this thermal cycle, the polymer granules completely melted down under the heat and pressure, and covered the sample entirely. The polymers subsequently solidified during the cooling part of the thermal cycle and formed a solid polymer block in which the samples were embedded. All four samples were mounted using this technique.

Figure 3.11: Remet IPA 30 Hot Mounting Machine [91]

3.3.5 Polishing Machine

After the mounting of the samples inside a polymer block, the cross section surface of the samples can easily be polished. The polishing of the samples is crucial for optical microscope imaging since a smooth and scratch-free surface allows a lot more detail to be observed across the cross section of the Mo samples. In order to achieve a smooth and scratch free surface, abrasive papers with progressively higher grit numbers were employed. During the polishing of the samples with abrasive papers, a Presi Mecatech 234 automatic polishing machine was used which is visible in Figure 3.12. The machine has a 250 mm rotating disk and a rotating head with four holes in which the samples were placed. Immediately after mounting, even the bottom surfaces of the Mo samples were covered with the mounting polymer. Because of this polymer layer, it was necessary to start from a very low grit number. The samples were polished using 80, 160, 400, 600, 800, 1000, 1200, 2000 and 4000 grit papers. During the polishing with abrasive papers, a steady supply of water was provided on the grinding papers. After the polishing with abrasive papers, the samples were further polished using polishing clothes and diamond suspensions. The particles sizes of the diamond suspensions used were 6 μm, 3 μm and 1 μm. After the diamond suspensions, the samples were polished for one final time using a 50/50 mixture of 0.25 μm silica suspension with water on another polishing cloth.

Figure 3.12: Presi Mecatech 234 Automatic Polishing Machine [92]

3.3.6 Optical Microscope

The optical microscope was used extensively throughout this research activity for several tasks. By using an optical microscope, it is possible to observe the samples with a lot more detail than through naked eye or a stereo microscope. By using a series of lenses and mirrors, optical microscope can magnify the details on the sample. Optical microscope was used for powder analysis, porosity analysis, grain structure analysis and Vickers hardness test. These tasks were accomplished through the usage of Leica DMI 5000 M optical microscope. The microscope is an inverted light optical microscope which is typically used for metallography. The microscope allows for magnification levels ranging from 50× to 1000×. Throughout this research magnification levels of 50×, 100×, 200×, and 500× were used for imaging to perform the aforementioned analyses. The Leica DMI 5000 M optical microscope which was used in this research activity can be seen in Figure 3.13.

3.3.7 Porosity Analysis and ImageJ Software

One of the main tasks of this research activity is to determine the internal porosity of the printed Mo samples. The porosity analyses was conducted by using the ImageJ software. The porosity analyses were performed by first taking the pictures of the cross-section of the Mo samples by using an optical microscope as mentioned in subsection 3.3.6. The porosity analysis was conducted based on fifteen images taken for each printed Mo sample. These images then got uploaded to the ImageJ software

Figure 3.13: Leica DMI 5000 M Optical Microscope [93]

for analysis. The images were first converted to 8-bit since the thresholding function works better for grayscale images. Then, through the usage of thresholding function, the area percentage of the porosities was calculated with the built in measure tool. It is possible to observe how thresholding function highlights the porosities within the material in Figure 3.14. The remaining solid areas are representative of the relative density of the printed material and the data are shown as such. These values were then used for mean porosity calculation for each sample in order to observe any effects of different rotation angles between each layer.

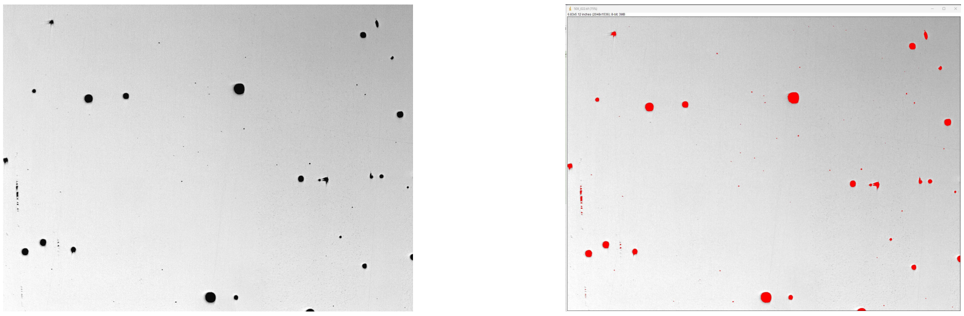

(a) Before Highlight **(b)** After Highlight

Figure 3.14: Thresholding function highlighting the internal porosities in red.

3.3.8 Microstructural Analysis

Another task to be completed for the printed Mo samples is to determine the nature of the microstructure of the samples. In order to be able to obtain more information about the grain structure of the material, the samples were imaged using an optical microscope at different magnification levels, namely 50×, 100×, 200×, and 500×. In order to enhance the microscope images, the samples need to be etched with an acidic solution. The acidic solution highlights the grains of the cross-section and makes the grains more distinguishable under the microscope. In order to etch the samples, two different acidic solutions were used. First acidic solution which was applied to samples 67-001 and 90-002, aimed to highlight the grains of these samples. The acidic solution consisted of 75 ml CH_3CH_2OH, 25 ml HCl and 50 ml of $FeCl_3 \cdot 6H_2O$ (1300 g/L solution at 50 °C). This acidic solution was applied to samples 67-001 and 90-002 by wetting their top surface for around 120 seconds and cleaning the surface with water afterwards. The second acidic solution is aimed to highlight the subgrains of the samples and was applied to samples 67-002 and 90-001. This acidic solution consisted of 25 ml HNO_3, 25 ml HF and 45 ml of water. This acidic solution was applied to the surface of the 67-002 and 90-001 for 15 seconds after being washed away with water. The acidic solutions highlighted the grains of the material as expected in which the grains were distinguishable as shown in Figure 3.15. After the etching, the samples were imaged under the optical microscope for microstructural analysis to be performed. The grain sizes of the 67-002 and 90-001 were measured using the Leica EZ4 W stereo microscope and the ImageJ software for a total of ten measurements that include the length and width measurements of individual grains in order to compare the average grain sizes of 90° and 67° rotation angle samples.

Figure 3.15: Samples after being etched by HF solution

3.3.9 Thermomechanical Analysis

Next task to be completed on the Mo samples is to determine the Coefficient of Thermal Expansion (CTE) of the Mo samples. To accurately determine the CTE, a Thermomechanical Analysis (TMA) needs to be performed. TMA is an analysis in which the dimensional changes happening to the sample are recorded as a function of temperature. The dimensional changes are monitored constantly by the TMA machine as the temperature inside the experiment chamber is increased gradually until the set temperature is reached. To perform the TMA analysis, SETSYS Evolution TMA machine which can be seen in Figure 3.16 was used during this research. SETSYS Evolution is machine capable of reaching temperatures up to 1600 °C under variable heating rates ranging from 0.1-100 °C/minute. A probe was set into contact with the samples in order to measure the dimensional changes happening to the sample. In this research activity, one sample was used for the CTE determination. The sample was heated to a temperature of 1400 °C and the dimensional changes were recorded and plotted in order to calculate the CTE of the sample.

Figure 3.16: SETSYS Evolution TMA Machine

3.3.10 Vickers Indentation Machine

Vickers hardness test is a type of test that is conducted on materials in order to determine the hardness of the material. The test involves indentation of the surface of the sample by using a pyramid shaped diamond indentor under a constant load. Afterwards, the diagonals of the indent can be measured under an optical microscope. The calculation of the Vickers Hardness Number (HV) is calculated by dividing the applied force by the surface area of the indentation mark. During the testing, a DHV-1000 Digital Microhardness Test Durameter was used in order to create the indentation. DHV-1000 is able to apply loads ranging from 10 gf to 1000 gf. During this research, a constant load of 1 kgf was applied for each sample and this load was applied for 10 seconds. The indentation process of the samples can be seen in 3.17. The indentation of the cross section started from the top along the build direction and each indent was created 1.25 mm below the previous one. For both the 90° and 67° samples a total of six indents were created by using the Vickers indentation machine. The diagonals of these indents were then measured by an optical microscope.

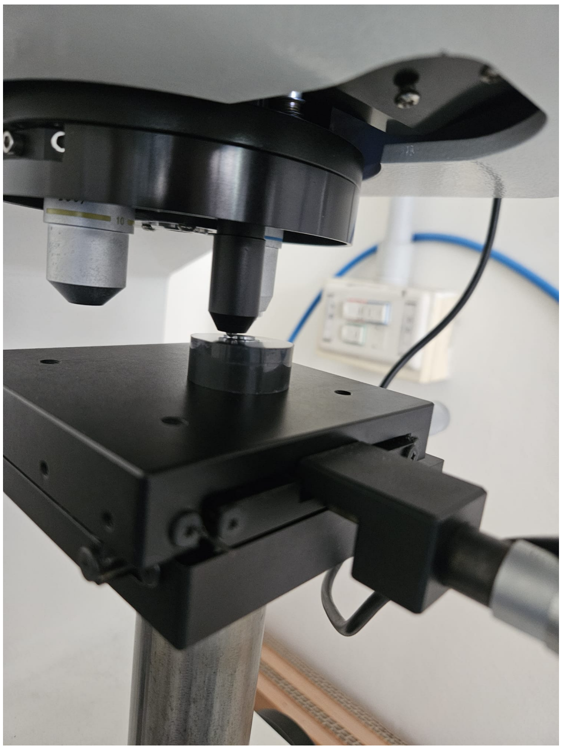

Figure 3.17: Indentation of the Mo samples using DHV-1000 Vickers indentation machine

Chapter 4

Results and Discussion

4.1 Powder Characterization Results

4.1.1 Flowability and Hausner Ratio Results

The flow characteristics of the Mo powder were measured by the Carney flow rate test in order to better understand the behavior of the Mo powder inside the PBF-EB machine where the powder was stored. Better flow characteristic of the Mo powder would ensure even and consistent spreading of the powder by the recoater blade as the PBF-EB machine creates subsequent layers. Thus, it is crucial to have a printing powder with good flow characteristics in order to improve the overall quality of the Mo powder. The results of the Carney flow rate test was reported in Table 4.1. Another measurement that creates a better understanding of the flow characteristics of Mo powder is the Hausner ratio calculation. The Hausner ratio is also used for explaining the powder's flow and packing characteristics that directly influence the behavior of the powder during the spreading of a new layer by the recoater blade. The results of the Hausner ratio calculation were reported in Table 3.1. When the results of the Hausner ratio measurement were compared against the Hausner ratio reference table in Table 3.1, it can be seen that the Mo powder that was used for the printing process had excellent flow characteristics.

By investigating the Hausner ratio and the Carney flow test, it was possible to reach one main observation:

- The Mo powder used in this research activity had excellent flow characteristics. Any defects or porosities that can be observed in the printed samples are unlikely to be caused due to the flow characteristics of the powder particles. The Mo powder was suitable for printing with the PBF-EB machine.

Table 4.1: Carney Flow Rate Test Results

Measurement	Time	Powder Amount
1	2.00	50 g
2	1.86	50 g
3	1.99	50 g
4	2.06	50 g
5	2.07	50 g
Average FR_C	1.996 s/50 g	
Standard Deviation	0.074993	

Table 4.2: Hausner Ratio Calculation

Measurement	Apparent Volume	Tap Volume	Hausner Ratio
1	8	7.5	1.067
2	8	7.5	1.067
3	8.5	8	1.063
Average Hausner Ratio			1.065
Standard Deviation			0.002

4.1.2 Skeletal Density Results

The skeletal density of the Mo powder that was used for printing the samples was calculated by a gas pycnometer. The pycnometer gives an accurate density measurement for the powder particles that are used in the printing operation. The pycnometer density measurement is a good indicator of the quality of the powder. If the density results obtained by the pycnometer are much lower than the theoretical density of Mo, it can be deducted that the powder particles have internal porosities or impurities with lower densities which can lead to a reduction in the quality of the printed samples. The results for the skeletal density analysis was reported in Table 4.3. The results of the skeletal density measurements can be compared to the theoretical density of pure Mo which was reported as 10.223 g/cm^3 in the literature [90].

By investigating the skeletal density of the Mo powder, it was possible to reach one main observation:

- The Mo powder had almost identical density to the reported theoretical density in the literature [90]. The results of the pycnometer suggests that the Mo powder had little to no internal porosities and the powder was suitable for printing with the PBF-EB machine.

Table 4.3: Skeletal Density Results

Measurement	Weight of Powders (g)	Volume of Powders (cm^3)	Density (g/cm^3)	Temperature ($°C$)
1	35.7099	3.4944	10.219	19.998
2	35.7099	3.4909	10.229	19.997
3	35.7099	3.4874	10.230	19.999
4	35.7099	3.4873	10.230	19.999
5	35.7099	3.4885	10.235	19.999
6	35.7099	3.4888	10.236	19.999
7	35.7099	3.4901	10.231	19.999
8	35.7099	3.4910	10.234	20.000
9	35.7099	3.4902	10.232	20.001
10	35.7099	3.4904	10.231	20.002
11	35.7099	3.4895	10.234	20.000
12	35.7099	3.4899	10.233	20.000
13	35.7099	3.4905	10.231	20.000
14	35.7099	3.4893	10.234	20.003
15	35.7099	3.4885	10.244	20.003
Average Skeletal Density (g/cm^3)			10.2359	
Standard Deviation			0.00598	

4.1.3 Powder Particle Characterization

The shape, size and morphology of the powder particles are crucial in determining the final properties of the printed samples using the PBF-EB method. The shape and morphology of the powder were investigated by optical microscope imaging. The optical microscope images revealed that the Mo powder particles are spherical in shape, in line with excellent flowability results uncovered in subsection 4.1.1. The microscope images which can be seen in Figures 4.1a and 4.1b, show the spherical shape of the powder particles.

Although a major part of the Mo powder is defect-free, while investigating the Mo powder under the optical microscope several defects were detected. These defects mainly consisted of internal porosities inside individual Mo powder particles. It is possible that these defects could influence the final properties of the printed Mo parts. An example of these internal porosities can be seen in Figures 4.2a and 4.2b in which the internal porosities were indicated by red arrows.

Another analysis that was conducted on the Mo samples is the XRD analysis that was conducted in order to investigate the composition of the Mo powder particles. The XRD machine created a graph with peaks and the corresponding θ angles of the diffracted X-rays. When the position of these peaks at different θ

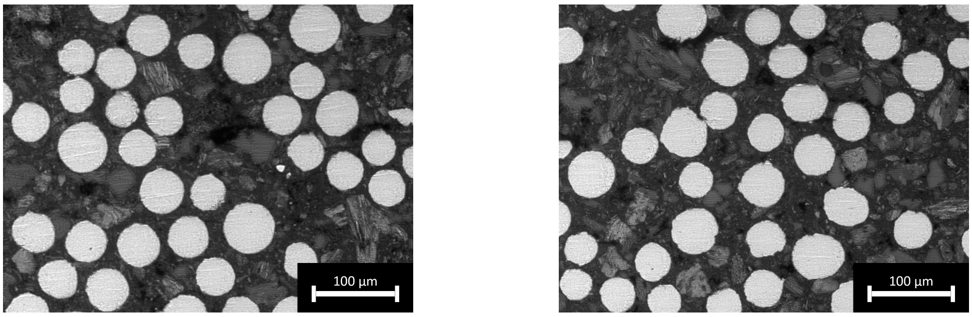

(a) **(b)**

Figure 4.1: Spherical powders imaged under the optical microscope at 200 × magnification

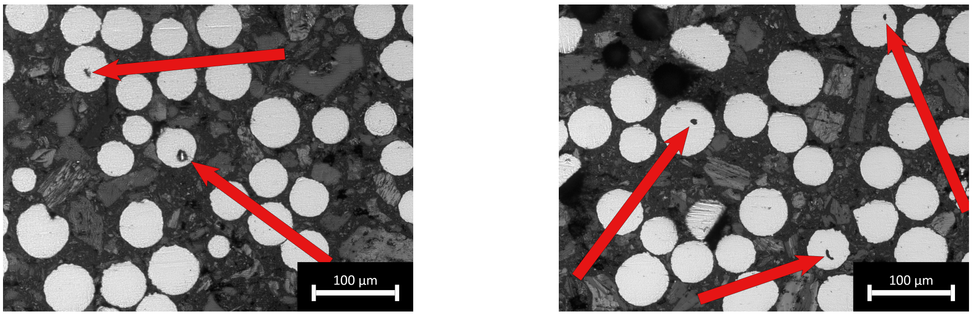

(a) **(b)**

Figure 4.2: Internal porosities of the Mo powders imaged under the optical microscope at 200 × magnification and indicated by red arrows

angles were compared to existing databases, the comparisons showed that the Mo powder used in the printing of the samples showed no traces of impurities. The XRD graph that was obtained from the powder samples is visible in Figure 4.3.

Next analysis that was conducted on the Mo samples was the ONH analysis in order to find out about especially the oxygen content of the Mo powder that was used for the printing. The results obtained from the ONH analysis showed that the Mo powder particles contained 190 ppm oxygen inside them. It is possible that the oxygen content that was found inside the Mo powder was responsible for some of the porosities found inside the powder particles and could also be related to some of the internal porosities that could be found in bulk samples.

Finally, the PSD of the Mo powder particles were investigated using the Laser diffraction particle size analyzer. The size of the powder particles are influential in

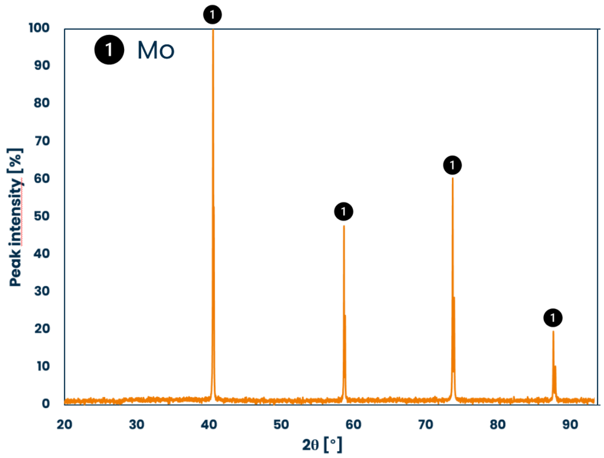

Figure 4.3: Results of the XRD analysis showing the composition is pure Mo.

determining the packing efficiency and the flowability of the Mo powder particles. Good flow characteristics result in more even spreading of the powder particles by the recoater blade and result in better overall quality of the part. In this study, a PSD curve and the relative D_{10}, D_{50} and D_{90} values were obtained. The PSD curve of the Mo powder can be seen in Figure 4.4 along with the relative D_{10}, D_{50} and D_{90} values in Table 4.4.

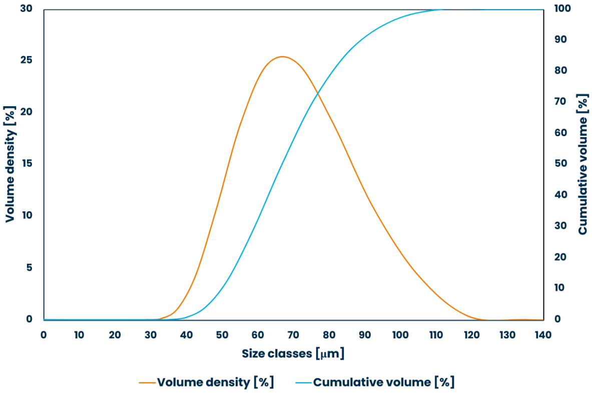

Figure 4.4: PSD Curve of the Mo powders

$$\begin{aligned} D_{10} &= 50\,\mu\mathrm{m} \\ D_{50} &= 67\,\mu\mathrm{m} \\ D_{90} &= 90\,\mu\mathrm{m} \end{aligned}$$

Table 4.4: PSD analysis percentile values

By characterizing the Mo powder, it was possible to reach three main observation:

- The Mo powder particles are spherical in shape which is crucial for good flow characteristics and helps create an even spreading of the powders. The PSD results showed that the obtained PSD was in line with the PSD that was provided by the producer [79].
- Although the majority of the Mo powder contained no visible defects under the optical microscope, several defective Mo particles that contained internal porosities were found. It is likely that these porosities were gas porosities and occurred due to the oxygen content that was found in the powder samples. It also is possible that these internal porosities could carry over to the bulk samples and create spherical gas porosities in the bulk Mo samples.
- The XRD analysis showed that the Mo powder contained no detectable impurities that can create internal defects in the bulk samples. The powders were suitable for printing pure Mo bulk samples.

4.2 Printed Sample Characterization Results

4.2.1 Top Surface Analysis

During this study, the stereo microscope images were used in order to investigate the surface characteristics and surface defects of the printed Mo samples that occurred in the macroscopic scale. The after-print surface quality of the sample should be adequately high in order to reduce the post processing needs. Higher quality surfaces would require less post processing thus require less time and cost for the manufacturer. It is also important to note that the post processing of the surface likely includes material removal through mechanical means and results in precious material loss. Therefore, it is important to optimize process parameters to achieve surface quality as high as possible. In this regard, the surface quality of the 67° and 90° rotation samples were investigated in order to determine the most suitable rotation angle for printing pure Mo.

Surface images of all four samples taken by the stereo microscope can be seen in Figure 4.5. It is clearly visible from the figure that the 90° rotation 90-001 and 90-002 samples have much smoother surface compared to 67° rotation 67-001 and 67-002 samples. The top surfaces of 67-001 and 67-002 samples were full of cavities left behind from the printing process. In comparison, it was not possible to observe cavities in the 90-001 and 90-002 samples as widespread as the 67-001 and 67-002 samples.

In order to further inspect the top surfaces of the Mo samples, it is necessary to magnify further with the stereo microscope. With higher magnification levels, it is possible to investigate smaller surface features on the top surface of the Mo samples. When the top surfaces of samples 67-001 and 67-002 were investigated at a higher magnification level, it was possible to obtain more information about the surface cavities. Higher magnification levels showed that these cavities were filled with unmelted residual powders inside. These unmelted powders are clearly visible in Figure 4.6. The figure shows the stereo images of 67-001 and 67-002 samples at 16× and 30× magnification levels. The unmelted powders inside the surface cavities were much easier to spot at higher magnification levels. Existence of unmelted powders inside these cavities might indicate that the surface cavities were caused by lack of fusion defects closer to the surface of the Mo samples.

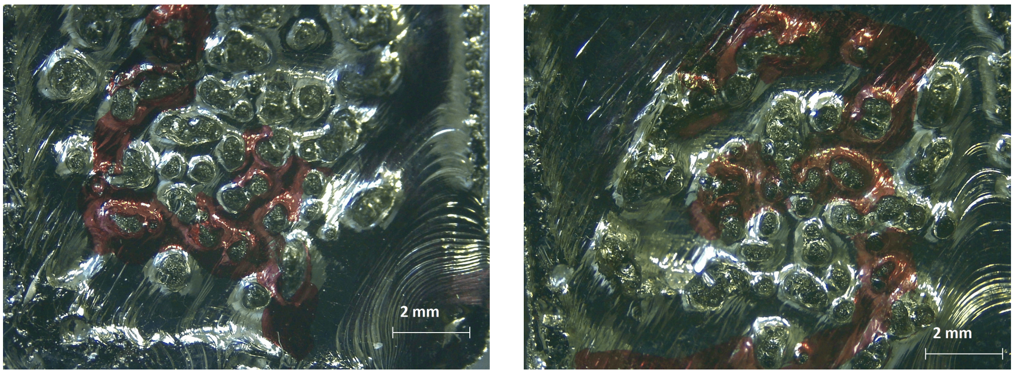

(a) Sample 67-002 **(b)** Sample 67-001

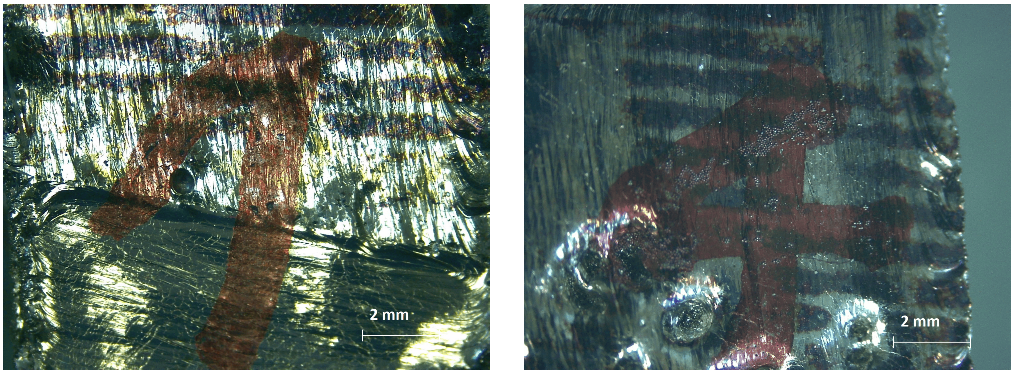

(c) Sample 90-001 **(d)** Sample 90-002

Figure 4.5: Stereo microscope images of the top surfaces of all 4 samples at 8× magnification

Similarly, the 90-001 and 90-002 samples were also investigated at higher magnification levels which is visible in 4.7. These higher magnification levels also revealed more details about the surface of the 90-001 and 90-002 samples printed with

90° beam rotation after each layer. The 90-001 and 90-002 surfaces had different surface morphologies compared to the 67-001 and 67-002 samples. Most significant difference is the lack of large cavities on the top surface. The top surfaces of 90-001 and 90-002 have a much smoother finish and a grid-like characteristic which cannot be observed on the surfaces of the 67-001 and 67-002 samples. Even though the top surfaces of the 90-001 and 90-002 had much higher quality than the 67-001 and 67-002 samples, it was still possible to observe several defects on the top surface. Figure 4.7c shows the residual unmelted powders on the surface of the 90-002 sample. However these unmelted powders were located on a smooth and flat surface unlike the 67-001 and 67-002 samples where the unmelted powders were located inside surface cavities. Figure 4.7d shows a large cavity on the surface of the Mo sample. This cavity has a smooth inner surface and no lack of fusion powders were located inside this cavity.

(a) Sample 67-001 at 16× magnification **(b)** Sample 67-001 at 30× magnification

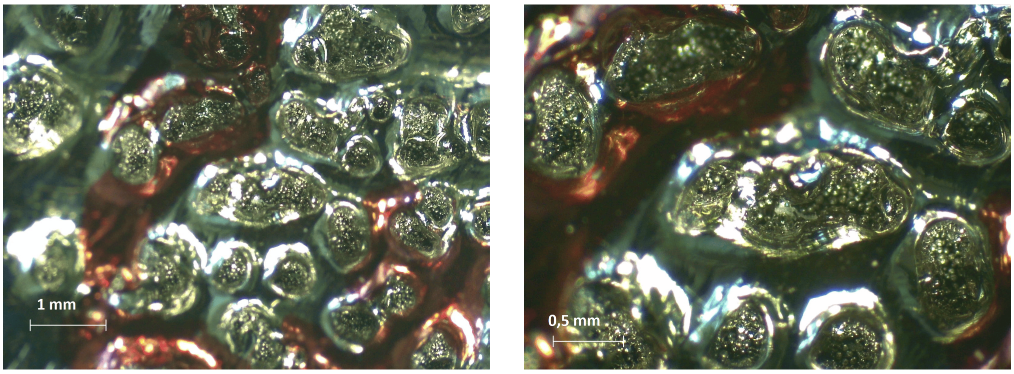

(c) Sample 67-002 at 16× magnification **(d)** Sample 67-002 at 30× magnification

Figure 4.6: Stereo microscope images of the top surfaces of 67-001 and 67-002 samples

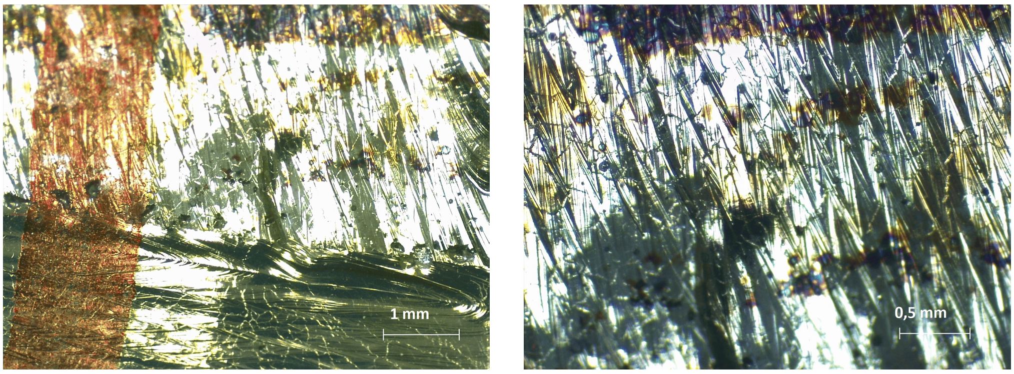

(a) Sample 90-001 at 16× magnification **(b)** Sample 90-002 at 30× magnification

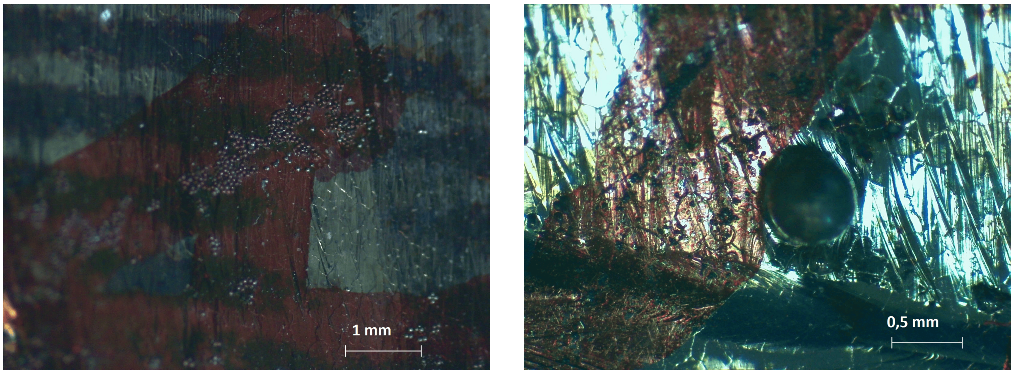

(c) Sample 90-002 at 16× magnification **(d)** Sample 90-002 at 30× magnification

Figure 4.7: Stereo microscope images of the top surfaces of 90-001 and 90-002 samples

By comparing the images taken with the stereo microscope, it was possible to reach two main observations:

- The 67° rotation samples had a much rougher surface morphology compared to the 90° rotation samples. This is evident by surface cavities spanning across the entire top surface area of the sample;
- Both the 90° and 67° rotation samples were susceptible to surface defects such as the residual unmelted powders on the surface. However, the amount of unmelted powders were much more numerous in 67° rotation samples in which internal surface of the surface cavities were filled with unmelted powders remaining from the printing operation.

4.2.2 Archimedes Density Analysis

Densities of all four samples were obtained using the Archimedes method and the density of each sample was calculated using Eq. 3.4. The Archimedes test is an important indication about the quality of the samples. It is desirable that the relative density of the printed material is as close as possible to Mo produced with conventional methods. It is important to have high density parts in order to demonstrate the feasibility of PBF-EB method for production of Mo parts. Another important aspect to this study specifically was to determine if there is a correlation between the rotation angle and the relative density. The correlation can indicate a more suitable rotation angle to be used for Mo samples in future work. The results that indicates each weight and density calculation can be seen in Table 4.5. The table indicates the dry weight average of each sample, submerged weight average of each sample, calculated bulk density of each sample and the relative density of each sample compared to the density of pure Mo 10.223 g/cm^3 [90].

Table 4.5: Bulk and Relative Density Data from Archimedes' Analysis

ID	**Dry Weight (g)**	**Submerged Weight (g)**	**Bulk Density (g/cm^3)**	**Relative Density (%)**
67-001	9.463	8.521	10.052	98.33
67-002	8.764	7.885	9.975	97.57
90-001	20.797	18.723	10.029	98.10
90-002	28.175	25.344	9.951	97.34

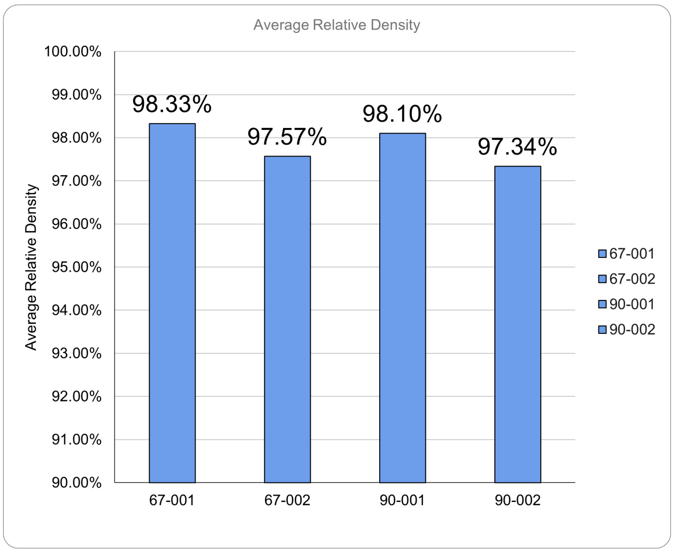

Figure 4.8: Average Relative Density of Each Sample

Figure 4.8 represents a comparison between the relative densities of each sample calculated in comparison to pure Mo.

By comparing the results of the Archimedes density analysis, it was possible to reach two main observations:

- It was possible to achieve high relative densities by using both the 67° and 90° rotation of the beam between each sample. This is indicated by higher than 97% relative density achieved by each sample;
- There was no clear indication of changing the rotation of the beam in each layer from 67° to 90° had significant effects on the Archimedes relative densities of the printed Mo sample.

4.2.3 Internal Porosity Analysis

Internal porosity of a sample refers to cavities and gaps hidden by the exterior walls of the printed Mo sample. Even though these porosities are not visible because of the outer shell of the material, these porosities still affect the properties of the material. These internal porosities are especially crucial for structural and load bearing parts because the porosities serve as stress concentrators in which the internal stresses of the material can be amplified in these regions and the yield strength of the material can be overcome. Another negative aspect of the internal porosities is that these regions accelerate the propagation of cracks as the cracks can pass through these areas of the material without any resistance. It is possible to have internal porosities in PBF-EB manufacturing due to several reasons. The first reason is the so called lack of fusion porosity in which the melt pools of the material do not properly wet the surrounding scan tracks or the underlying solid layer which creates gaps inside the material. Another porosity type is the key hole porosity in which a high power beam creates a very deep and narrow vapor cavity called a keyhole due to metal evaporation. If this keyhole is not stable enough, it can collapse on itself and create a gap inside the materials interior. The final porosity type is gas porosities, in which trapped gasses inside the material leave behind spherical voids as they escape due to high temperatures.

Table 4.6: Average Density and Porosity Values of Mo samples

ID	Average Internal Porosity	Average Relative Density	Standard Deviation
67-001	0.63%	99.37%	0.007
67-002	0.87%	99.13%	0.008
90-001	0.76%	99.24%	0.005
90-002	1.18%	98.82%	0.014

The results of the internal porosity and density calculations can be seen in Table 4.6. The table indicates the internal porosity percentage calculated by the threshold function of the ImageJ software and the derived average density values from the internal porosities in different columns. All four samples achieved a high relative density that is above 98% for all samples that were printed.

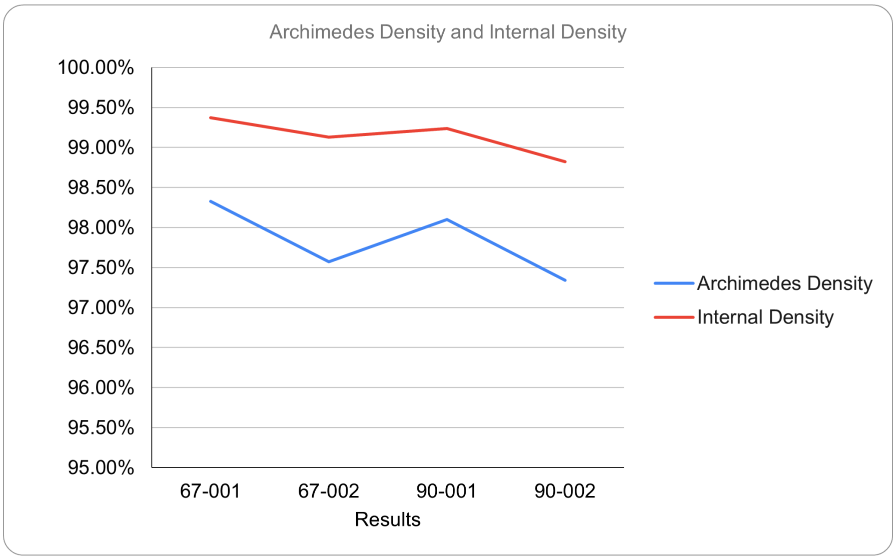

Figure 4.9: Archimedes Relative Density and Internal Porosity Analysis Results

The calculated internal porosity values were then plotted together with the relative density results obtained from the Archimedes density analysis. The comparison of the two plots is visible in Figure 4.9. Even though the relative density results obtained from the internal porosity analysis were slightly higher than the Archimedes relative density analysis, it can be seen that the two plots followed the same trend.

After the density analysis was conducted, the optical microscope images were investigated further in order to better understand the nature of the porosities and the internal structure of the printed Mo samples. A large majority of the internal porosities were spherical in nature. These spherical porosities were observable all across the internal structure of all four printed Mo samples. The spherical porosities were in general smaller in diameter, smaller than 100 μm in most cases. Examples of these aforementioned spherical porosities can be observed in Figure 4.10. These spherical porosities are typical of gas porosities due to their spherical shape and small diameter.

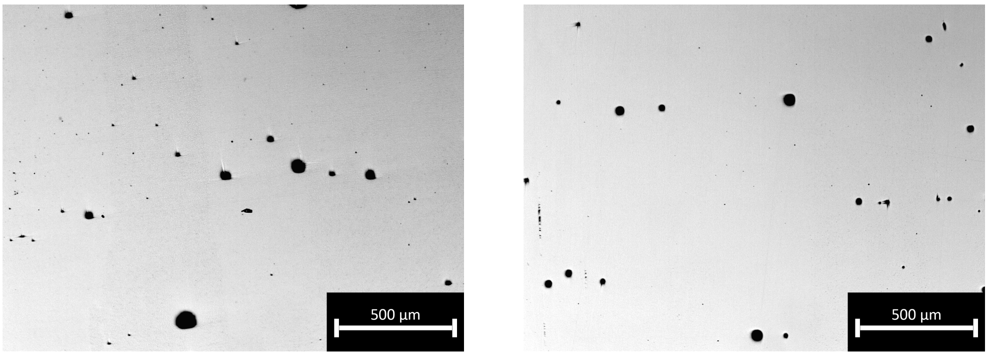

(a) Spherical Porosities inside 90-001 at 50× magnification **(b)** Spherical Porosities inside 90-002 at 50× magnification

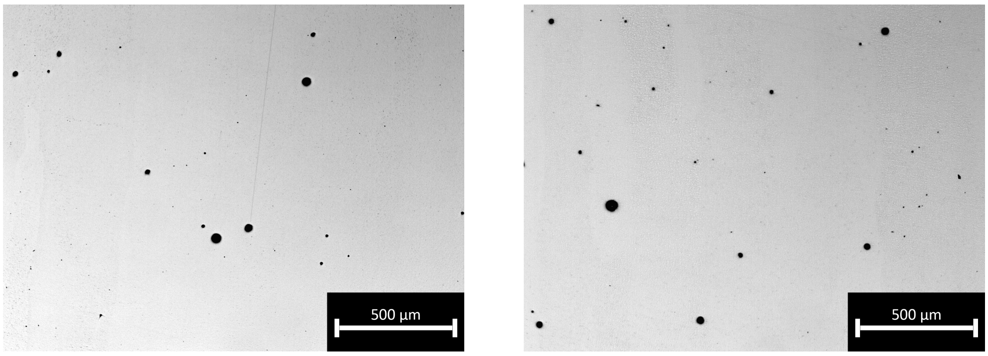

(c) Spherical Porosities inside 67-001 at 50× magnification **(d)** Spherical Porosities inside 67-002 at 50× magnification

Figure 4.10: Optical microscope images of the spherical porosities located inside all four samples

By comparing the images taken with the optical microscope, it was possible to reach three main observations:

- Both the 90° and 67° rotation angle samples were able to achieve very high relative density levels above 98%. This proves that the PBF-EB process is suitable for printing pure Mo samples with high relative density at both the 90° and 67° rotation angles;
- The relative density analysis results followed the same trend with the Archimedes density analysis results which reinforce the idea that the density results were correctly measured.
- The main type of porosity defect that was detected in the microstructure was the small sized spherical porosities. These type of porosities are typical of

gas porosities in which the trapped gasses inside the building block escape through the printed Mo part and leave these spherical porosities.

4.2.4 Microstructural Analysis

Next analysis that was conducted is the microstructural analysis, specifically the investigation of the grain structure of the printed Mo material. For polycrystalline materials such as Mo, the grain structure is one of the most influential factors determining the mechanical properties of the printed parts such as the tensile strength, ductility or fracture toughness. The grain structure of the material is defined mainly by the size, morphology and the orientation of the grains. In general, it is desirable to have a fine grain structure since reducing the size of the grains improves the mechanical properties of the part as defined by Hall-Petch equation. Another factor is the morphology of the grains itself, if it is desirable for the printed part to have isotropic mechanical properties, it is important the grains are equiaxed in order to have the same properties in every direction.

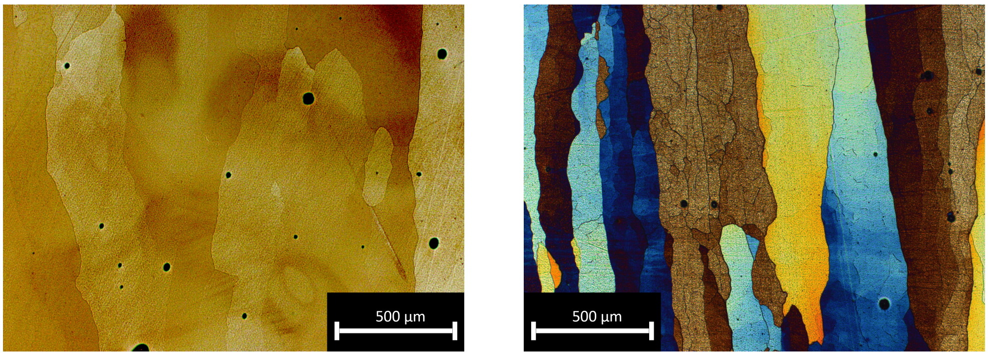

(a) Grain Structure of 67-001 at 50× magnification

(b) Grain Structure of 67-002 at 50× magnification

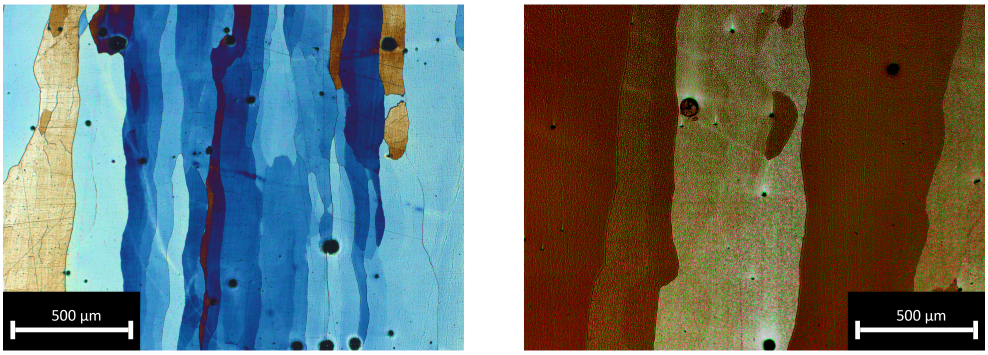

(c) Grain Structure of 90-001 at 50× magnification

(d) Grain Structure of 90-002 at 50× magnification

Figure 4.11: Optical microscope images of the grain boundaries of all four samples

The analysis of the grains of the samples was conducted by optical microscope after the samples were etched with an acidic solution. Through the acidic etching, the grains became more suitable for imaging as it can be seen in Figure 4.11.

All four Mo samples were determined to have columnar grains stretching across the entire cross section in the building direction of the Mo samples. The columnar grains are aligned with the heat flux of the process which is parallel to the building direction from the base of the building platform towards the top surface of the sample. The reason for the nature of the heat flux is caused due to the fact that the high heat created by the EB is located at the top and the heat gradually moves towards the base of the sample. By using higher magnification levels of the optical microscope, it was possible to observe more details about the grain structure of the Mo samples. At higher magnification levels, it was easier to detect that the columnar grains are composed of subgrain structures which were created by the thermal stresses that occured due to the high heating and cooling rates of PBF-EB process. The detected subgrain structures were indicated by arrows and visible in Figure 4.12.

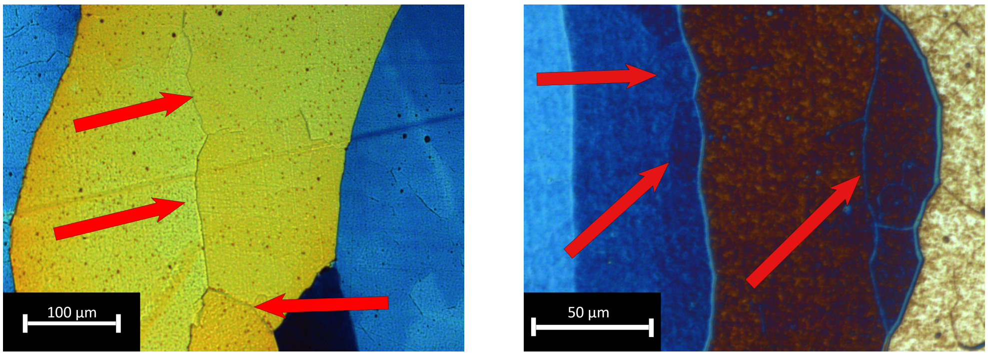

(a) Subgrain of 67-002 at 200× magnification

(b) Subgrains of 67-002 at 500× magnification

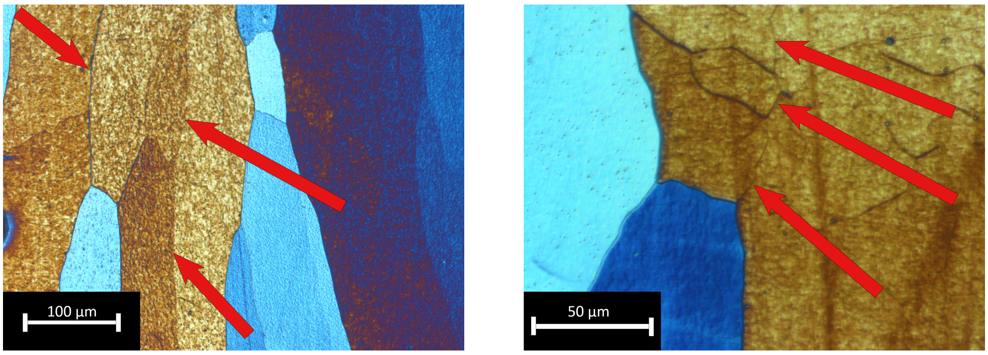

(c) Subgrains of 90-001 at 200× magnification

(d) Subgrains of 90-001 at 500× magnification

Figure 4.12: Subgrains of 90-001 and 67-002 samples pointed out by red arrows

The images for the grain size measurements were taken by the stereo microscope and the measurements were conducted by the ImageJ software. The length and width measurements of the 90° and 67° rotation samples are visible in Table 4.7. The average length and width measurements for the samples 90-001 and 67-002 are visualized in Figures 4.13 and 4.14. When the average lengths and widths of the grains of the samples 90-001 and 67-002 are compared, it is possible to see there are no significant differences in the grain sizes when the rotation angle of the EB is changed.

Table 4.7: Grain Size Measurements for Samples 90-001 and 67-002

	90-001		67-002	
Measurement	Length (μm)	Width (μm)	Length (μm)	Width (μm)
1	1783.586	166.920	2329.823	183.614
2	2627.995	227.618	3623.045	157.849
3	1980.636	210.889	2559.892	237.088
4	2837.146	269.454	2146.978	164.954
5	2942.387	174.672	2344.752	196.052
6	3100.514	167.608	1839.667	187.089
7	2292.366	243.266	2677.113	258.395
8	3340.779	198.577	1940.215	208.004
9	3133.866	250.379	3137.822	197.103
10	1229.158	168.454	1923.896	227.901
Average	2526.844	207.784	2492.370	200.023
Standard Dev	685.485	38.430	610.113	32.924

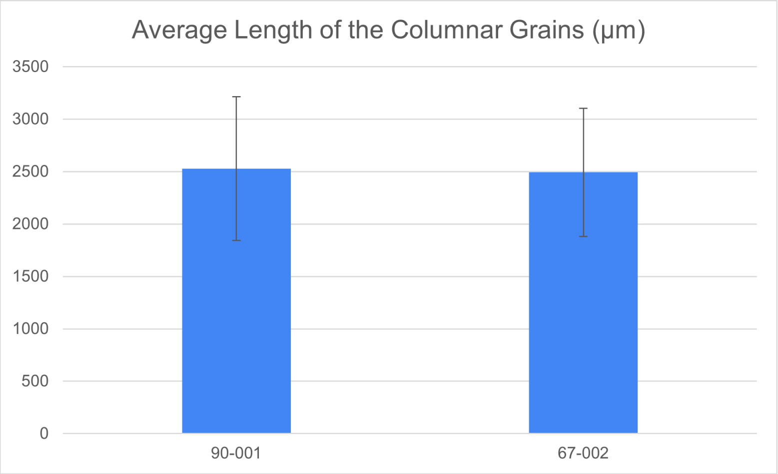

Figure 4.13: Average length of the grains of Samples 90-001 and 67-002

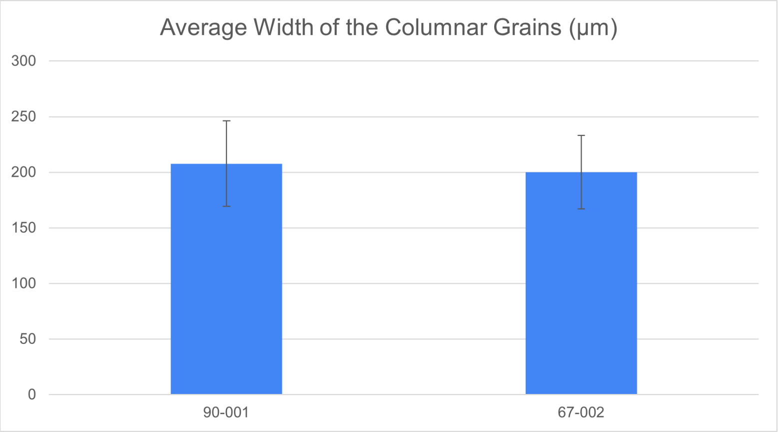

Figure 4.14: Average width of the grains of Samples 90-001 and 67-002

By comparing the images taken with the optical and stereo microscopes, it was possible to reach three main observations:

- Both the 90° and 67° rotation angle samples showed columnar grains stretching all across the length of the sample in the building direction. The columnar grains were created due to the direction of the heat flux in which the heat flows from the high temperature top layer of the sample where the EB is working, towards the base of the sample where the lowest temperatures can be detectable.

- In both the 90° and 67° rotation angle samples, it was possible to observe subgrain structures inside the main grains of the Mo metal. The subgrain structures occurs due to high thermal stresses that occur during the PBF-EB process. High heating and cooling rates that is achieved due to the high energy beam can contribute to subgrain formation. The effect of the rotation angle was minimal to the microstructure since all four samples showed columnar grains with subgrain structures aligned in the building direction.

- When the grain sizes of the 90° and 67° rotation angle samples were compared, it was seen that changing the rotation angle between 90° and 67° rotation angles showed almost no effect on the grain size of the overall cross-section of the Mo samples. It can be suggested that different rotation angles are not influential when determining the final grain size.

4.2.5 Thermomechanical Analysis

The final analysis conducted on this research activity was the Thermomechanical Analysis specifically to determine the CTE of the printed Mo samples. As discussed in Section 2.5, one of the main application of Mo is the high temperature applications in which high temperature resistance is crucial. Due to this, it is essential to know the behavior of the printed Mo samples at elevated temperatures. CTE is a material property which describes the dimensional changes of the parts as a function of temperature. Understanding the CTE of the material, especially at elevated temperatures, is paramount since any unpredictable dimensional changes of constrained parts in elevated temperatures can have catastrophic effects. The CTE of one of the Mo samples is calculated inside a TMA machine and the results were plotted as a function of temperature. The Figure 4.15 describes the change in CTE as a function of the environment temperature. The measured CTE was 6.424 $10^{-6}K^{-1}$ at 1000 °C which is in line with the CTE values in literature [94].

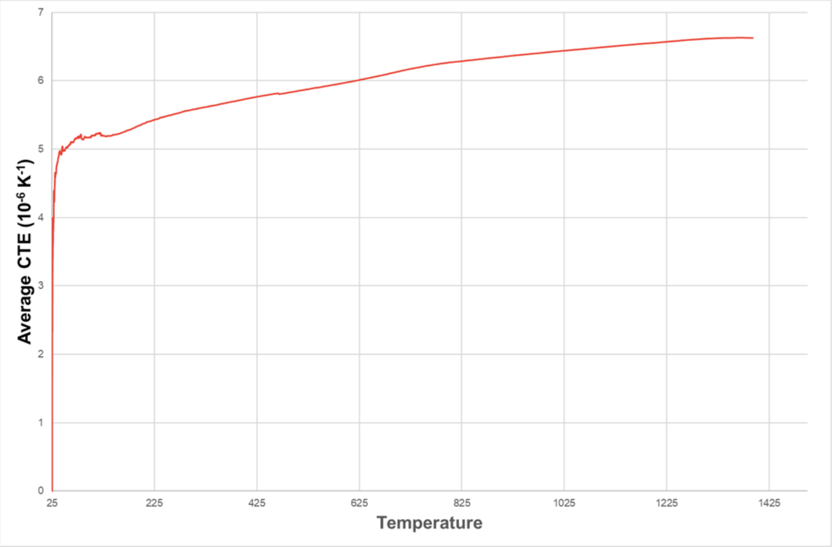

Figure 4.15: Change in CTE as a function of temperature

Through the data provided by the TMA machine, it was possible to make the following claim:

- The printed Mo samples were heated up to 1400 °C in order to observe the CTE changes as a function of time. The Mo sample showed CTE values in line with the CTE values that can be found in the literature. The predictability of the CTE values reinforced the suitability of pure Mo parts which were printed with the PBF-EB method, to be used for elevated temperature applications.

4.2.6 Vickers Hardness Test

The hardness test results were obtained after indentations were created by the Vickers indentation machine and the axes of the diamond indents were measured with an optical microscope. The Vickers hardness test is an important parameter in order to determine the quality of the Mo parts. In the literature Vickers hardness number of pure Mo is indicated as 156 HV [95]. It is important that the parts produced by the PBF-EB method have higher or comparable Vickers hardness to the indicated hardness value. Comparable or higher hardness values can indicate that high quality Mo parts can be manufactured using the PBF-EB method. Another aspect is to determine how the hardness of the material is affected by the change in the rotation angle between each layer. If there is a correlation between the hardness, it is important to determine this relationship which gives future activities a clear understanding on which rotation angle is more suitable according to the needs of the application. The results of the Vickers hardness test can be seen in Table 4.8. The table indicates the number of measurements that was conducted for each sample and the Vickers hardness measurements for each indent. The mean of these hardness values were calculated and indicated below the measurements.

Table 4.8: Vickers Hardness Measurements for Each Sample (HV)

67-001 Hardness (HV)		**67-002 Hardness (HV)**	
Meas.	**Value**	**Meas.**	**Value**
1	168.58	1	173.66
2	162.57	2	166.90
3	163.74	3	169.21
4	164.83	4	178.19
5	157.19	5	181.99
6	168.07	6	180.92
67-001 Average: 164.16 HV		**67-002 Average: 175.15 HV**	

90-001 Hardness (HV)		**90-002 Hardness (HV)**	
Meas.	**Value**	**Meas.**	**Value**
1	167.94	1	166.36
2	158.88	3	162.84
3	155.08	5	170.91
4	151.28	7	165.73
5	163.96	9	165.16
6	160.43	10	164.75
90-001 Average: 159.54 HV		**90-002 Average: 165.66 HV**	

Mean hardness measurements can be used for comparing the hardness values of each sample. The mean values were used for creating the 4.16 in which it was possible to visually compare the hardness values of each sample and discover a correlation between the hardness measurements and the change of rotation angle after each layer. From the figure, it is possible to see that the 67° rotation samples have slightly higher Vickers hardness numbers when compared to the 90° rotation samples.

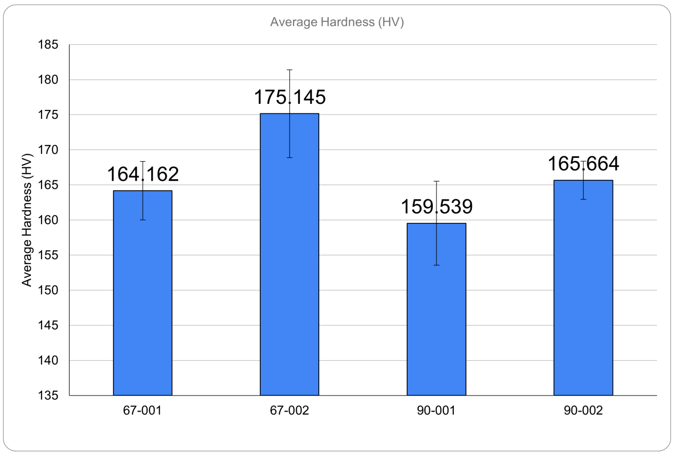

Figure 4.16: Average Hardness Values of Each Sample

By comparing the results of the Vickers Hardness test, it was possible to reach two main observations:

- Samples printed with both the 90° and 67° rotation angles achieved up to 12.27% higher Vickers hardness numbers when compared to pure Mo. It can be argued that these higher Vickers hardness values make the PBF-EB method a candidate for applications that call for high hardness Mo parts.
- When the Vickers hardness numbers of both 90° and 67° rotation angle samples were compared, it can be seen that the 67° rotation samples had slightly higher Vickers hardness numbers. The hardness difference was visualized in Figure 4.16.

Chapter 5

Conclusions

This thesis aimed to investigate the feasibility of producing Mo parts by using PBF-EB method and also to investigate the effects of 90° and 67° rotation angle on the final properties of the material. In order to achieve these two goals, extensive analyses were conducted on the powder particles and the final printed Mo samples. This study showed that the PBF-EB method is suitable for producing Mo parts with low defects and good mechanical properties. The effects of the rotation angle were minimal on the final properties of the Mo samples and both the 90° and 67° rotation angles are suitable for production.

Additionally, the following results were obtained through the experiments performed in this research activity:

- By using the Freemelt One PBF-EB machine with 1080 W beam power, 400 mm/s beam speed, 0.12 mm line offset, 0.07 mm layer thickness processing parameters, it was possible to produce Mo parts with high relative densities above 98% by using both the 90° and 67° rotation angles of the beam. The high relative densities achieved also suggest that PBF-EB method is suitable for Mo production providing an effective manufacturing method with low cycle times and low need for post processing when compared to traditional production methods of Mo.

- The printed Mo samples had a low amount of internal porosities as low as 0.63% of the cross section. In this study, it was also uncovered through optical microscope imaging that some of the starting powders also contained internal porosities. It can be suggested that some of the internal porosities are caused by the existence of oxygen and already present porosities in the starting powders and it can be possible to achieve higher relative densities when using Mo powders that contain lower amount of internal defects and oxygen.

- One of the main differences between the 90° and 67° rotation angle samples were observed when the morphology of the top surface was observed by stereo microscope. The 90° rotation angle sample showed a higher quality top surface with minimal defects thus required less post processing and was more ready to use. 67° rotation angle samples on the other hand contained surface cavities filled with unmelted powders and they required the post processing of the top surface in order to remove the cavity defects.

- Both the 90° and 67° rotation angle samples were observed to have columnar grains when observed under the optical microscope after acidic etching. The columnar grains stretched the length of the sample in the building direction and it was possible to observe subgrain structures that occurred due to high thermal stresses. The size of the grains in both the 90° and 67° samples were extremely close and it is possible to suggest that using different rotation angles had minimal effect on the grain size of the printed samples. The grains of the 90° rotation angle sample on average had 2526.844 μm length and 207.784 μm width. The grains of the 67° rotation angle sample on average had 2492.370 μm length and 200.023 μm width.
- The Vickers hardness tests showed that both the 90° and 67° rotation angle samples had superior hardness (up to 12.27%) when compared to the hardness of pure Mo. The Vickers hardness results showed that the 67° rotation angle samples had higher Vickers hardness although these improvements to the hardness were minimal. The hardness test results suggested that the PBF-EB method could be the desirable manufacturing method for producing Mo parts that require higher hardness in the application area.The usage of the PBF-EB method could eliminate the need for further strengthening steps in order to reach the desired mechanical properties.

Further studies in this area should be done and should focus on comparing other scanning strategies such as spot melting or helix scanning in order to obtain more information about the effects of different scanning strategies when printing Mo with the PBF-EB method. Further improvements to the quality of the final parts can be done by adjusting the printing parameters of the PBF-EB machine and using different Mo powders that contain lower amount of internal defects.

Bibliography

[1] Hans-Joachim Lunk and Hans Hartl. «Discovery, properties and applications of molybdenum and its compounds». In: *Transition Metal Chemistry* 42.8 (2017), pp. 731–764. DOI: `10.1007/s11243-017-0171-0` (cit. on pp. 1, 16).

[2] W. Knabl, G. Leichtfried, and R. Stickler. «Refractory Metals and Refractory Metal Alloys». In: *Springer Handbook of Materials Data*. Springer, 2018, pp. 307–337. DOI: `10.1007/978-3-319-69743-7_13` (cit. on pp. 1, 16).

[3] John A. Shields. *Applications of Molybdenum Metal and its Alloys*. Technical Report. London, UK: International Molybdenum Association (IMOA), 2013 (cit. on pp. 1, 16, 17).

[4] R. E. Gold. «Refractory metal alloys for fusion reactor applications». In: *Journal of Nuclear Materials* 85–86 (1979), pp. 805–815. DOI: `10.1016/0022-3115(79)90359-3` (cit. on pp. 1, 16).

[5] J. Wang, C. Liu, T. Lu, R. Fu, T. Xu, Z. Li, C. Jing, and Y. Cui. «Microstructure and mechanical properties of unalloyed molybdenum fabricated via wire arc additive manufacturing». In: *International Journal of Refractory Metals and Hard Materials* 107 (2022), p. 105886. DOI: `10.1016/j.ijrmhm.2022.105886` (cit. on p. 1).

[6] Encyclopaedia Britannica, Inc. *Molybdenum*. Accessed: Sep. 24, 2025. 2025. URL: `https://www.britannica.com/science/molybdenum` (cit. on p. 2).

[7] J. L. Johnson and T. Palmer. «Directed energy deposition of molybdenum». In: *International Journal of Refractory Metals and Hard Materials* 84 (2019), p. 105029. DOI: `10.1016/j.ijrmhm.2019.105029` (cit. on p. 2).

[8] ISO/ASTM. *ISO/ASTM 52900:2021 – Additive Manufacturing — General Principles — Fundamentals and Vocabulary*. Standard. Geneva, Switzerland / West Conshohocken, PA, USA, 2021 (cit. on pp. 2, 8).

[9] ASTM International. *Standard Terminology for Additive Manufacturing Technologies*. West Conshohocken, PA, USA, Mar. 2012 (cit. on pp. 2, 9, 10).

[10] Ian Gibson, David Rosen, Brent Stucker, and Mahyar Khorasani. *Additive Manufacturing Technologies*. 3rd ed. Cham, Switzerland: Springer, 2021 (cit. on pp. 3, 8–10, 12).

[11] P. Rebesan, M. Ballan, M. Bonesso, and M. Vedani. «Pure Molybdenum Manufactured by Laser Powder Bed Fusion: Thermal and Mechanical Characterization at Room and High Temperature». In: *Additive Manufacturing* 47 (2021), p. 102277. DOI: `10.1016/j.addma.2021.102277` (cit. on p. 3).

[12] S. Di Sturco, Giulio Marchese, Federica Bondioli, Mariangela Lombard, Daniele Ugues, Paolo Fino, and Sara Biamino. «Understanding the processability, microstructure, and properties of molybdenum processed by Electron Beam Powder Bed Fusion (EB-PBF)». In: *Materials & Design* (2025). DOI: `10.1016/j.matdes.2025.xxx` (cit. on pp. 3, 18).

[13] J. Braun, L. Kaserer, I. Letofsky-Papst, K.-H. Leitz, H. Kestler, and G. Leichtfried. «On the role of carbon in molybdenum manufactured by Laser Powder Bed Fusion». In: *International Journal of Refractory Metals and Hard Materials* 92 (2020), p. 105283. DOI: `10.1016/j.ijrmhm.2020.105283` (cit. on p. 3).

[14] P. Fernandez-Zelaia, C. Ledford, E. A. I. Ellis, Q. Campbell, A. Márquez Rossy, D. N. Leonard, and M. M. Kirka. «Crystallographic texture evolution in electron beam melting additive manufacturing of pure Molybdenum». In: *Materials & Design* 207 (2021), p. 109809. DOI: `10.1016/j.matdes.2021.109809` (cit. on pp. 3, 18).

[15] Sanjay Kumar. «Electron Beam Powder Bed Fusion». In: *Additive Manufacturing Processes*. Ed. by Sanjay Kumar. Cham, Switzerland: Springer International Publishing, 2020, pp. 65–78. DOI: `10.1007/978-3-030-45089-2_4` (cit. on pp. 4, 12–14).

[16] S. A. Bansal, V. Khanna, and P. Gupta. *Metal Matrix Composites Fabrication, Production, and 3D Printing*. Vol. 1. CRC Press, 2023 (cit. on p. 4).

[17] H. Jia, H. Sun, H. Wang, Y. Wu, and H. Wang. «Scanning Strategy in Selective Laser Melting (SLM): A Review». In: *The International Journal of Advanced Manufacturing Technology* 113.9-10 (2021), pp. 2413–2435. DOI: `10.1007/s00170-021-06810-3` (cit. on pp. 5, 6, 11).

[18] L. N. Carter, C. Martin, P. J. Withers, and M. M. Attallah. «The influence of the laser scan strategy on grain structure and cracking behaviour in SLM powder-bed fabricated nickel superalloy». In: *Journal of Alloys and Compounds* 615 (2014), pp. 338–347. DOI: `10.1016/j.jallcom.2014.06.172` (cit. on p. 5).

[19] Y. M. Arisoy, L. E. Criales, T. Ozel, B. Lane, S. Moylan, and A. Donmez. «Influence of scan strategy and process parameters on microstructure and its optimization in additively manufactured nickel alloy 625 via laser powder bed fusion». In: *The International Journal of Advanced Manufacturing Technology* 90 (5 2017), pp. 1393–1417. DOI: `10.1007/s00170-016-9429-z` (cit. on p. 5).

[20] J. Shi C. Lu and V. Maitra. «Modelling and process optimization for relative density of Ti6Al4V produced by selective laser melting: a data-driven study». In: *The International Journal of Advanced Manufacturing Technology* 121 (3 2022), pp. 1973–1988. DOI: `10.1007/s00170-022-09453-0` (cit. on p. 6).

[21] Todd Grimm. *User's Guide to Rapid Prototyping*. Dearborn, MI, USA: Society of Manufacturing Engineers, 2004, p. 55 (cit. on p. 8).

[22] Osama Abdulhameed, Abdulrahman Al-Ahmari, Syed Hammad Mian, et al. «Additive Manufacturing: Challenges, Trends, and Applications». In: *Heliyon* 5.12 (2019), e02810. DOI: `10.1016/j.heliyon.2019.e02810` (cit. on p. 9).

[23] Ugur M. Dilberoglu, Bahar Gharehpapagha, Ulas Yaman, and Melik Dolen. «The Role of Additive Manufacturing in the Era of Industry 4.0». In: *Procedia Manufacturing* 11 (2017), pp. 545–554 (cit. on p. 9).

[24] M. Braian, D. Jönsson, M. Kevci, and A. Wennerberg. «Geometrical accuracy of metallic objects produced with additive or subtractive manufacturing: A comparative in vitro study». In: *Dental Materials* 34.7 (2018), pp. 978–993. DOI: `10.1016/j.dental.2018.03.009` (cit. on p. 9).

[25] U. M. Dilberoğlu, B. Gharehpapagh, U. Yaman, and M. Dölen. «Current trends and research opportunities in hybrid additive manufacturing». In: *The International Journal of Advanced Manufacturing Technology* 113 (Jan. 2021). Critical Review, published 27 January 2021, pp. 623–648 (cit. on p. 9).

[26] M. P. Sealy, G. Madireddy, R. E. Williams, P. Rao, and M. Toursangsaraki. «Hybrid processes in additive manufacturing». In: *Journal of Manufacturing Science and Engineering* 140.6 (2018). Published June 1, 2018. DOI: `10.1115/1.4038644` (cit. on p. 9).

[27] Sadettin Cem Altıparmak, Victoria A. Yardley, Zhusheng Shi, and Jianguo Lin. «Extrusion-based additive manufacturing technologies: State of the art and future perspectives». In: *Journal of Manufacturing Processes* 83 (2022), pp. 607–636. DOI: `10.1016/j.jmapro.2022.09.016` (cit. on p. 9).

[28] Hossein Taheri, Mohammad Rashid Bin Mohammad Shoaib, Lucas W. Koester, Timothy A. Bigelow, Peter C. Collins, and Leonard J. Bond. «Powder-Based Additive Manufacturing – A Review of Types of Defects, Generation Mechanisms, Detection and Evaluation Metrology». In: *International Journal of Additive and Subtractive Materials Manufacturing* 1 (2017). Art. no. 088204. DOI: `10.1504/IJASMM.2017.088204` (cit. on pp. 10, 11).

[29] Rajinth Shanthar, Kun Chen, and Chamil Abeykoon. «Powder-based additive manufacturing: A critical review of materials, methods, opportunities and challenges». In: *Advanced Engineering Materials* (2023). Advance online publication, 28Jun2023. DOI: `10.1002/adem.202300375` (cit. on p. 10).

[30] Haniyeh Fayazfar, Mehrnaz R. Salarian, Allan Rogalsky, Dyuti Sarker, Paola Russo, Vlad Paserin, and Ehsan Toyserkani. «A Critical Review of Powder-Based Additive Manufacturing of Ferrous Alloys: Process Parameters, Microstructure and Mechanical Properties». In: *Materials & Design* 144 (Apr. 2018), pp. 98–128. DOI: `10.1016/j.matdes.2018.02.018` (cit. on pp. 10, 14).

[31] Michał Olejarczyk, Piotr Gruber, Małgorzata Gazińska, Anna Krokos, Grzegorz Ziółkowski, Patrycja Szymczyk-Ziółkowska, Emilia Grochowska, and Tomasz Kurzynowski. «New powder reuse schema in laser-based powder bed fusion of polymers». In: *Waste Management* 187 (July 2024), pp. 11–21. DOI: `10.1016/j.wasman.2024.06.030` (cit. on p. 11).

[32] E. Soylemez, J. L. Beuth, and K. Taminger. «Controlling Melt Pool Dimensions Over a Wide Range of Material Deposition Rates in Electron Beam Additive Manufacturing». In: (Aug. 2010), pp. 571–582 (cit. on p. 11).

[33] Divyansh Singh Dev, Mahender Thotakuri, and Avala Raji Reddy. «Powder bed fusion process: A brief review». In: *Materials Today: Proceedings* 46.Part 1 (2021), pp. 350–355. DOI: `10.1016/j.matpr.2020.08.415` (cit. on p. 11).

[34] Ratnadeep Paul and Sam Anand. «Process energy analysis and optimization in selective laser sintering». In: *Journal of Manufacturing Systems* 31.4 (2012), pp. 429–437. DOI: `10.1016/j.jmsy.2012.07.004` (cit. on p. 11).

[35] J.-P. Kruth, X. Wang, T. Laoui, and L. Froyen. «Lasers and materials in selective laser sintering». In: *Assembly Automation* 23.4 (2003), pp. 357–371. DOI: `10.1108/01445150310698652` (cit. on p. 11).

[36] L. Liu, Y. Wang, Z. Chen, X. Li, Q. Zhao, and J. Yang. «State-of-the-art of selective laser melting process: A review». In: *Journal of Manufacturing Systems* 62 (2022), pp. 394–409. DOI: `10.1016/j.jmsy.2022.06.005` (cit. on p. 11).

[37] Jyotirmoy Nandy, Hrushikesh Sarangi, and Seshadev Sahoo. «A Review on Direct Metal Laser Sintering: Process Features and Microstructure Modeling». In: *Lasers in Manufacturing and Materials Processing* 6.6 (2019), pp. 280–316. DOI: `10.1007/s40516-019-00094-y` (cit. on p. 11).

[38] Michael Baumers, Christopher Tuck, and Richard Hague. *Selective Heat Sintering Versus Laser Sintering: Comparison of Deposition Rate, Process Energy Consumption and Cost Performance*. Technical Report. Available: UT Austin Repository. University of Texas at Austin, 3D Printing Research Group, Faculty of Engineering, University of Nottingham, 2015 (cit. on p. 11).

[39] R. Singh et al. «Powder Bed Fusion Process in Additive Manufacturing: An Overview». In: *Materials Today: Proceedings* 26 (2020), pp. 3058–3070. DOI: `10.1016/j.matpr.2020.02.635` (cit. on p. 11).

[40] J. Raute, A. Beret, M. Biegler, and M. Rethmeier. «Life cycle assessment in additive manufacturing of copper alloys—comparison between laser and electron beam». In: *Welding in the World* 68 (2024), pp. 3169–3176. DOI: `10.1007/s40194-024-01856-9` (cit. on p. 12).

[41] S. Megahed, V. Aniko, and J. H. Schleifenbaum. «Electron Beam-Melting and Laser Powder Bed Fusion of Ti6Al4V: Transferability of Process Parameters». In: *Metals* 12.8 (2022), p. 1332. DOI: `10.3390/met12081332` (cit. on p. 12).

[42] Charles Kittel. *Introduction to Solid State Physics*. 7th ed. Wiley, 1996 (cit. on p. 12).

[43] A. N. Broers. «Electron Gun using Long-Life Lanthanum Hexaboride Cathode». In: *Journal of Applied Physics* 38.3 (1967), pp. 1991–1995. DOI: `10.1063/1.1709807` (cit. on p. 12).

[44] Ralf Edinger. «Additive Manufacturing – Enhancing Build Resolution and Expanding Build Sizes with G-Code Programmable Laser-Heated Variable 150kV Electron Beam Gun». In: *Proceedings of the Society of Vacuum Coaters Conference*. Aug. 2019. DOI: `10.14332/svc19.proc.0029` (cit. on p. 12).

[45] Freemelt AB. *Freemelt® ONE: The 3D printer tailored for materials research and development*. `https://freemelt.com/freemelt-one/`. Accessed: Jul. 2025. 2025 (cit. on pp. 13, 19, 26).

[46] M. Sigl, S. Lutzmann, and M. F. Zäh. «Transient Physical Effects in Electron Beam Sintering». In: *2006 International Solid Freeform Fabrication Symposium (SFF)*. Austin, TX, USA, 2006, pp. 464–477 (cit. on p. 13).

[47] S. Vock, B. Kloden, A. Kirchner, T. Weißgärber, and B. Kieback. «Powders for Powder Bed Fusion: A Review». In: *Progress in Additive Manufacturing* 4.4 (2019), pp. 383–397. DOI: `10.1007/s40964-019-00078-6` (cit. on p. 13).

[48] Arcam AB / GE Additive. *Arcam EBM® Corporate Brochure (v3.0)*. Archived at Web Archive. Available at: Web Archive snapshot from Aug. 18, 2018. Accessed: Jul. 2025. 2018. URL: `https://web.archive.org/web/20180818032238/http://www.arcam.com/wp-content/uploads/arcamebm-corp-brochure-fnlv3.pdf` (cit. on p. 13).

[49] F. I. Azam, A. M. A. Rani, K. Altaf, T. V. V. L. N. Rao, and H. A. Zaharin. «An In-Depth Review on Direct Additive Manufacturing of Metals». In: *IOP Conference Series: Materials Science and Engineering.* Vol. 328. 2018, p. 012005. DOI: `10.1088/1757-899X/328/1/012005` (cit. on p. 13).

[50] M. A. Lodes, R. Guschlbauer, and C. Körner. «Process development for the manufacturing of 99.94% pure copper via selective electron beam melting». In: *Materials Letters* 143 (2015), pp. 298–301. DOI: `10.1016/j.matlet.2014.12.105` (cit. on p. 14).

[51] D. Wang, C. Wei, Y. Zhang, C. Kou, and J. Fan. «Multiple stages of smoking phenomenon in electron-beam powder-bed fusion process». In: *Additive Manufacturing* 66 (2023), p. 102877. DOI: `10.1016/j.addma.2023.102877` (cit. on p. 14).

[52] Zongwen Fu and Carolin Körner. «Actual state-of-the-art of electron beam powder bed fusion». In: *European Journal of Materials* 2.1 (2022), pp. 54–116. DOI: `10.1080/26889277.2022.2040342` (cit. on p. 14).

[53] Z. C. Cordero, H. M. Meyer, P. Nandwana, and R. R. Dehoff. «Powder Bed Charging during Electron-Beam Additive Manufacturing». In: *Acta Materialia* 124 (2017), pp. 437–445. DOI: `10.1016/j.actamat.2016.11.012` (cit. on p. 14).

[54] A. Klassen, V. E. Forster, V. Juechter, and C. Körner. «Numerical simulation of multi-component evaporation during selective electron beam melting of TiAl». In: *Journal of Materials Processing Technology* 247 (2017), pp. 280–288. DOI: `10.1016/j.jmatprotec.2017.04.003` (cit. on p. 14).

[55] S. Chikosha, L. C. Tshabalala, H. Bissett, M. Lesufi, N. K. Mnguni, T. M. Motsai, T. Manama, and S. Hoosain. «Spheroidisation of Stainless Steel Powder for Additive Manufacturing». In: *Metals* 11.7 (2021), p. 1081. DOI: `10.3390/met11071081` (cit. on p. 14).

[56] Taher Abu-Lebdeh, Ransford Damptey, Vincent Lamberti, and Sameer Hamoush. «Powder Packing Density and Its Impact on SLM-Based Additive Manufacturing». In: *TMS 2019 148th Annual Meeting Exhibition Supplemental Proceedings.* Ed. by Taher Abu-Lebdeh, Ransford Damptey, Vincent Lamberti, and Sameer Hamoush. The Minerals, Metals Materials Series. Springer, 2019, pp. 355–367. DOI: `10.1007/978-3-030-05861-6_33`. URL: `https://link.springer.com/chapter/10.1007/978-3-030-05861-6_33` (cit. on p. 14).

[57] H. Gruber, M. Henriksson, E. Hryha, and L. Nyborg. «Effect of Powder Recycling in Electron Beam Melting on the Surface Chemistry of Alloy 718 Powder». In: *Metallurgical and Materials Transactions A* 50 (2019), pp. 4410–4422. DOI: `10.1007/s11661-019-05333-7` (cit. on p. 14).

[58] Stanford Advanced Materials. *Spherical Molybdenum Powder.* `https://www.samaterials.com/spherical-molybdenum-powder.html`. Accessed: Jul. 14, 2025 (cit. on p. 14).

[59] C. Körner. «Additive manufacturing of metallic components by selective electron beam melting—A review». In: *International Materials Reviews* 61.5 (2016), pp. 361–377. DOI: `10.1080/09506608.2016.1176289` (cit. on p. 15).

[60] P. M. Cordero, J. Mireles, S. Ridwan, and R. B. Wicker. «Evaluation of monitoring methods for electron beam melting powder bed fusion additive manufacturing technology». In: *Progress in Additive Manufacturing* 2 (2017), pp. 1–10. DOI: `10.1007/s40964-016-0015-6` (cit. on p. 15).

[61] L. E. Murr et al. «Microstructures and properties of solid and reticulated mesh components of pure iron fabricated by electron beam melting». In: *Journal of Materials Research and Technology* 2.4 (2013), pp. 376–385. DOI: `10.1016/j.jmrt.2013.10.002` (cit. on p. 15).

[62] C. Botero, W. Sjöström, E. Jimenez-Pique, A. Koptyug, and L.-E. Rännar. «Small- to Large-Scale Electron Beam Powder Bed Fusion of Functionally Graded Steels». In: *Journal of Manufacturing and Materials Processing* 9.1 (2025), p. 7. DOI: `10.3390/jmmp9010007` (cit. on p. 15).

[63] I. A. Segura, J. Mireles, D. Bermudez, C. A. Terrazas, L. E. Murr, K. Li, V. S. Y. Injeti, R. D. K. Misra, and R. B. Wicker. «Characterization and mechanical properties of cladded stainless steel 316L with nuclear applications fabricated using electron beam melting». In: *Journal of Nuclear Materials* 507 (2018), pp. 164–176. DOI: `10.1016/j.jnucmat.2018.04.026` (cit. on p. 15).

[64] W. J. Davids, M. J. D. H. de Boer, R. L. de Kloe, and J. J. M. A. de Hosson. «Phase transformation pathways in Ti-6Al-4V manufactured by electron beam powder bed fusion». In: *Acta Materialia* 213 (2021), p. 116981. DOI: `10.1016/j.actamat.2021.116981` (cit. on p. 15).

[65] M. Shao, J. Zhang, J. Wang, Y. Zhang, W. Zhang, and J. Wang. «The effect of beam scan strategies on microstructural variations in Ti-6Al-4V fabricated by electron beam powder bed fusion». In: *Materials Design* 191 (2020), p. 108587. DOI: `10.1016/j.matdes.2020.108587` (cit. on p. 15).

[66] D. Pan, Z. Zhang, J. Zhang, X. Zhang, Y. Zhang, and J. Wang. «Enhanced strength and ductility of nano-TiBw-reinforced Ti matrix composites fabricated by electron beam powder bed fusion». In: *Additive Manufacturing* 48 (2022), p. 102482. DOI: `10.1016/j.addma.2022.102482` (cit. on p. 15).

[67] L. E. Murr et al. «Microstructures and mechanical properties of electron beam rapid manufactured Ti-6Al-4V biomedical prototypes compared to wrought Ti-6Al-4V». In: *Materials Characterization* 60.2 (2009), pp. 96–105. DOI: `10.1016/j.matchar.2008.07.006` (cit. on p. 15).

[68] M. Luo, X. Zhang, Y. Zhang, J. Zhang, J. Wang, and W. Zhang. «Grain boundary network evolution in electron-beam powder bed fusion of Inconel 738». In: *Materials Science and Engineering: A* 865 (2024), p. 114114. DOI: `10.1016/j.msea.2023.114114` (cit. on p. 16).

[69] G. L. Knapp, N. Raghavan, A. Plotkowski, and T. DebRoy. «Experiments and simulations on solidification microstructure for Inconel 718 in powder bed fusion electron beam additive manufacturing». In: *Additive Manufacturing* 25 (2019), pp. 511–521. DOI: `10.1016/j.addma.2018.12.001` (cit. on p. 16).

[70] Y. Yao, C. Xing, H. Peng, H. Guo, and B. Chen. «Solidification microstructure and tensile deformation mechanisms of selective electron beam melted Ni3Al-based alloy at room and elevated temperatures». In: *Materials Science and Engineering: A* 802 (2021), p. 140629. DOI: `10.1016/j.msea.2020.140629` (cit. on p. 16).

[71] A. Hinojos, J. Mireles, A. Reichardt, P. Frigola, P. Hosemann, L. E. Murr, and R. B. Wicker. «Joining of Inconel 718 and 316 Stainless Steel using electron beam melting additive manufacturing technology». In: *Materials Science and Engineering: A* 674 (2016), pp. 1–10. DOI: `10.1016/j.msea.2016.07.019` (cit. on p. 16).

[72] N. N. Greenwood and A. Earnshaw. *Chemistry of the Elements*. English. 2nd ed. Butterworth-Heinemann, 1997. ISBN: 978-0-7506-3365-9. DOI: `10.1016/C2009-0-30414-6` (cit. on p. 16).

[73] IUPAC. *IUPAC Periodic Table of the Elements*. `https://iupac.org/what-we-do/periodic-table-of-elements/`. Accessed: 2025-07-05. 2024 (cit. on p. 16).

[74] International Molybdenum Association (IMOA). *Molybdenum market information*. `https://www.imoa.info/molybdenum/molybdenum-market-information.php`. Accessed: 2025-07-05. 2025 (cit. on p. 16).

[75] T. DebRoy et al. «Additive manufacturing of metallic components – Process, structure and properties». In: *Progress in Materials Science* 92 (2018), pp. 112–224. DOI: `10.1016/j.pmatsci.2017.10.001` (cit. on p. 16).

[76] Robert E. Smallwood, ed. *Refractory Metals and Their Industrial Applications: A Symposium*. Philadelphia, PA, USA: American Society for Testing and Materials, 1968, pp. 12–13 (cit. on p. 17).

[77] U.S. Geological Survey. *Mineral Commodity Summaries.* Tech. Rep. Washington, DC, USA: U.S. Department of the Interior, Jan. 2025 (cit. on pp. 17, 18).

[78] Fathi Habashi, ed. *Handbook of Extractive Metallurgy.* Vol. 2. Weinheim, Germany: Wiley-VCH, 1997, p. 1372 (cit. on p. 18).

[79] Metalpine GmbH. *Mo - Metalpine - The Art of Spherical Powders.* Accessed: Nov. 7, 2025. Metalpine GmbH. 2025. URL: `https://metalpine.at/product/mo/` (cit. on pp. 19, 42).

[80] ASTM International. *Standard Test Methods for Flow Rate of Metal Powders Using the Carney Funnel.* ASTM B964/B964M. West Conshohocken, PA, 2025 (cit. on pp. 19, 20).

[81] ASTM International. *Standard Test Methods for Flow Rate of Metal Powders Using the Hall Flowmeter Funnel.* ASTM B213/B213M. West Conshohocken, PA, 2025 (cit. on p. 19).

[82] United States Pharmacopeia and National Formulary (USP-NF). *Powder Flow.* General Chapter <1174>. Official: May 1, 2024. Rockville, MD, USA: United States Pharmacopeial Convention, May 2024 (cit. on pp. 20, 21).

[83] R. Boyle. *New Experiments Physico-mechanicall: Touching the Spring of the Air, and Its Effects (made, for the Most Part, in a New Pneumatical Engine).* Oxford, England: Printed by H. Hall, Printer to the University, for Tho. Robinson, 1660 (cit. on p. 21).

[84] Anton Paar. *Gas Pycnometer for Semi-Solid and Solid Density: Ultrapyc.* Accessed: Nov. 7, 2025. Anton Paar. 2025. URL: `https://www.anton-paar.com/corp-en/products/details/ultrapyc/` (cit. on p. 22).

[85] Malvern Panalytical. *Mastersizer | Laser Diffraction Particle Size Analyzers.* Accessed: Nov. 7, 2025. Malvern Panalytical Ltd. 2025. URL: `https://www.malvernpanalytical.com/en/products/product-range/mastersizer-range` (cit. on p. 22).

[86] Malvern Panalytical. *Empyrean - X-ray Diffractometers.* Accessed: Nov. 7, 2025. Malvern Panalytical Ltd. 2025. URL: `https://www.malvernpanalytical.com/en/products/product-range/empyrean-range` (cit. on pp. 23, 24).

[87] LECO Corporation. *836 Series: Elemental Analysis for Oxygen, Nitrogen, and Hydrogen Detection.* Accessed: Nov. 10, 2025. LECO Corporation. 2025. URL: `https://www.leco.com/products/836-series/` (cit. on p. 25).

[88] Leica Microsystems. *Leica EZ4 W & EZ4 E Educational stereo microscopes for college & university.* Accessed: Oct. 24, 2025. Oct. 2025. URL: `https://www.leica-microsystems.com/products/light-microscopes/stereo-microscopes/p/leica-ez4-w/` (cit. on p. 27).

[89] PRESI. *Mecatome T210.* Accessed: Oct. 26, 2025. 2022. URL: `https://www.presi.com/en/product/mecatome-t210/` (cit. on p. 28).

[90] J. W. Arblaster. *Selected Values of the Crystallographic Properties of the Elements.* Materials Park, OH: ASM International, 2018. ISBN: 978-1-62708-154-2 (cit. on pp. 29, 38, 46).

[91] REMET. *IPA 30 - 40 - 50 - 60.* Accessed: Oct. 26, 2025. REMET. 2025. URL: `https://remet.it/products/ipa-30` (cit. on p. 31).

[92] PRESI. *Métallographie par PRESI : Analyse et coupe Métallographique.* Accessed: Oct. 26, 2025. PRESI. 2022. URL: `https://www.presi.com/` (cit. on p. 32).

[93] Leica Microsystems. *DMI5000 M Microscopio da ricerca invertito per l'analisi dei materiali.* Accessed: Oct. 29, 2025. Leica Microsystems. 2025. URL: `https://www.leica-microsystems.com/it/prodotti/microscopi-ottici/p/leica-dmi5000-m/` (cit. on p. 33).

[94] Ultra-High Temperature Materials I: Carbon (Graphene/Graphite) and Refractory Metals. «Carbon (Graphene/Graphite) and Refractory Metals». In: *Ultra-High Temperature Materials I.* Publisher Name, if known, 2014 (cit. on p. 54).

[95] G. V. Samsonov. «Mechanical Properties of the Elements». In: *Handbook of the Physicochemical Properties of the Elements* (cit. on p. 55).